Development of pure-rotational coherent Raman spectroscopy on hydrogen for applied flame thermometry.

T. M. Klijn Velderman

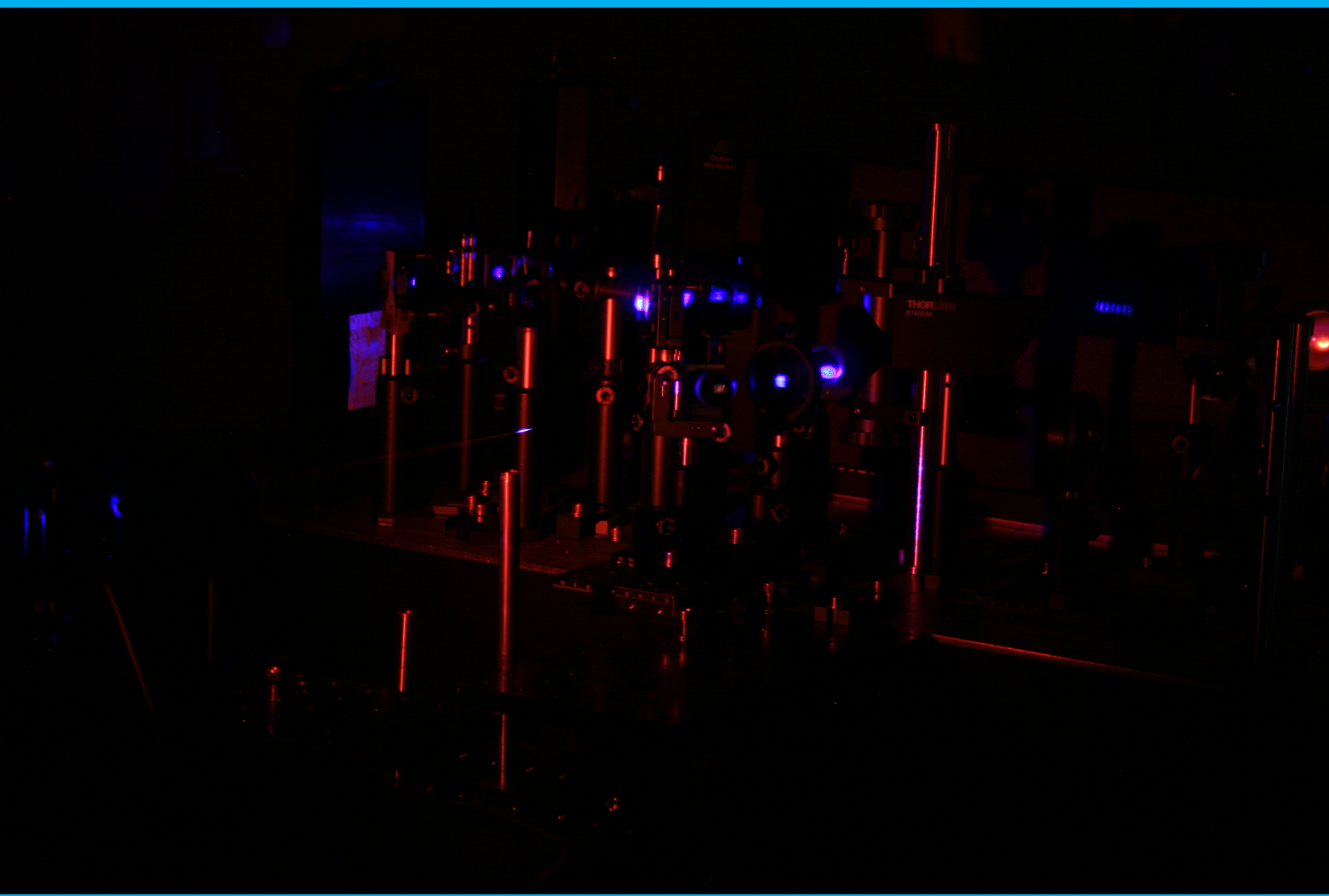

Development of pure-rotational coherent Raman spectroscopy on hydrogen for applied flame thermometry.

by

T. M. Klijn Velderman

to obtain the degree of Master of Science
at the Delft University of Technology,
to be defended publicly on Friday April 30th, 2021 at 13:00 PM.

Student number:	4601564	
Project duration:	March 1, 2020 – April 30, 2021	
Thesis committee:	Prof. dr. ir. Alexis Bohlin	TU Delft, supervisor
	Dr. ir. Dmitrii Kliukin	TU Delft, supervisor
	Prof. dr. ir. Mark Tummers	TU Delft, co-supervisor
	Prof. dr. ir. Dirk Roekaerts	Chair Assessment Committee

An electronic version of this thesis is available at http://repository.tudelft.nl/.

Abstract

Work is presented on a novel hybrid fs/ps two beam CARS application for spatiotemporal gas phase hydrogen thermometry, capable of sampling at a rate of 1 kHz. The aim of the research is to assess the feasibility of directly probing hydrogen for accurate temperature measurements in a combustion environment. Typically, nitrogen is used in applied CARS thermometry because of the inert nature of the gas and the availability on both the products- and reactants side of the flame. Nitrogen is well understood in CARS applications and is therefore used as a benchmark for the results obtained through hydrogen thermometry. No hydrogen was available in the lab, so a rich premixed methane-air flame was used in a regular Bunsen burner. At high equivalence ratio's sufficient amounts of hydrogen are formed as an intermediate species to be probed in the flame. Quantum-mechanical models were used to predict the molecular responses of the corresponding molecules, after which they are compared to the experimental data. The feasibility of hydrogen thermometry was assessed through a series of three different experiments: using the standard output pulse of the regenerative amplifier at 35 fs for spatiotemporal measurements, using the 35 fs pulse for point measurements, and using a frequency broadened 10 fs pulse produced through filamentation for point measurements. Nitrogen and hydrogen spectra were recorded simultaneously to ensure proper data comparison. The 1 kHz acquisition rate enabled the evaluation of temporal correlation in the temperature data. The spatiotemporal CARS measurements clearly depicted flame dynamics at 1 Hz and 12Hz, but the signal to noise ratio in the hydrogen signal was too weak to properly assess the data. The point measurements using the 35 fs pulse yielded similar average temperatures, but the precision in the hydrogen temperatures was poor (25%) due to the fact that only the first two S-branch transition in hydrogen were excited. In the experiments using the 10 fs pulse, the first four S-branch transitions in hydrogen were excited. This greatly improved the precision for the temperature measurements (2%), surpassing that of the nitrogen thermometry (4%). The nitrogen and hydrogen temperatures also showed great temporal correlation (0.85-0.9). However, there was a very consistent temperature deficit in the hydrogen temperatures of 550K, most like caused by a wavelength dependence in the optics (which are optimized for narrowband applications) which severely affects the higher Raman shifted hydrogen signal. Lastly, an experiment was done using the 10 fs pulse to probe O-branch transitions in hydrogen, and a serious discrepancy between the CARS and CSRS spectra were found, again likely caused by the optics in the setup. These results approximated nitrogen temperatures much better, within 7% at 2000 K. Overall, the results were promising, but not yet conclusive and more research is needed.

Contents

List of Figures

List of Tables

1

Introduction

The thin layer of gases around our planet, otherwise known as the Earth's atmosphere, is what enables humans and millions of other life forms to live here. The atmosphere provides breathable oxygen vital to a large part of life on earth. Furthermore, the atmosphere protects against harmful ultra-violet radiation and traps a portion of incoming solar radiation in the form of heat, keeping Earth at a temperature suitable for its current inhabitants. The entrapment of solar radiation is done by the absorption of long wave radiation by various molecules in our atmosphere, most notably H_2O, and noncondensing gases like CO_2, CH_4, N_2O, O_3, and lastly aerosols (sulphates, nitrates, dust, soot and other carbonaceous aerosols) [2]. Of these constituents, H_2O and CO_2 are the largest contributors in absorbing long wave radiation, absorbing 75% (50% through water vapour and 25% through clouds) and 20% respectively. The remaining 5% is absorbed by the other (noncondensing) gases mentioned earlier. These numbers make it seem as if H2O is the main culprit in the greenhouse effect. However, because water will readily condense or evaporate depending on ambient air temperature, pressure and saturation, it is part of a self-regulating fast feedback loop that largely dictates local temperatures. CO_2, on the other hand, is a well-mixed gas that does not condense or precipitate from the atmosphere [3]. Its effect on temperature is much more gradual and global and has direct (no feedback) consequences. This identifies CO2 as the main contributor to the greenhouse effect and global warming.

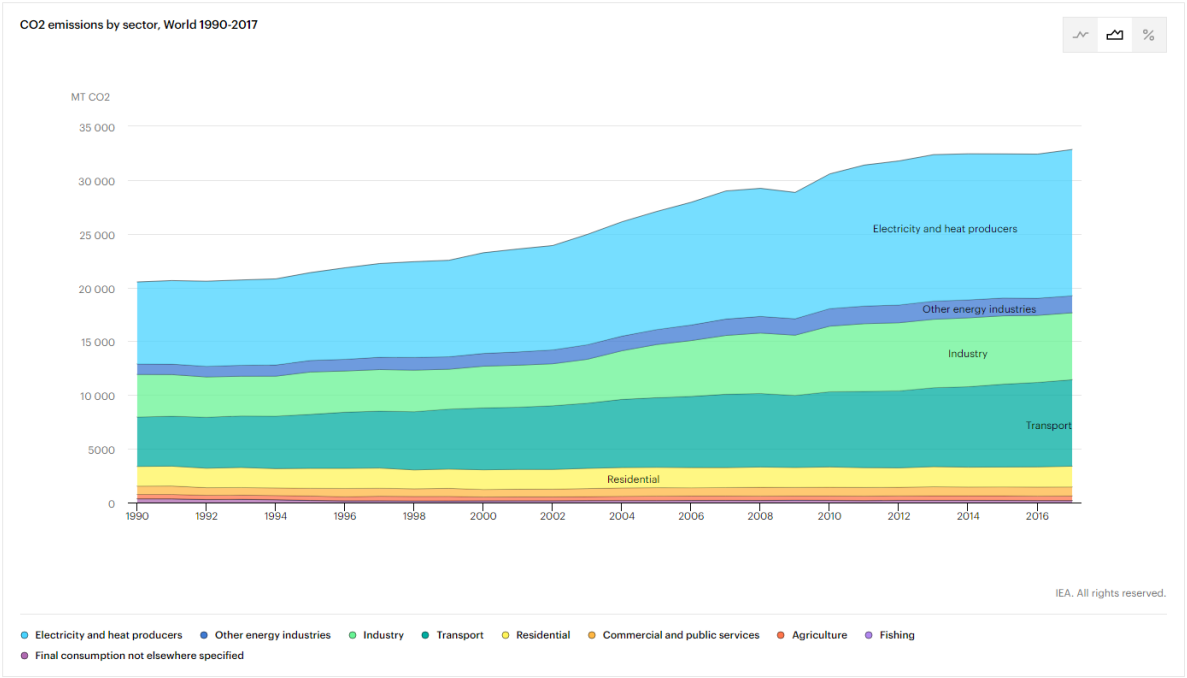

Figure 1.1: Breakdown of CO_2 emissions by sector over the years (International Energy Agency) [5]

Since the industrial revolution of 1750, the CO_2 and CH_4 levels in the atmosphere have increased by 35% and 148% respectively [4]. As can be seen from figure 1.1, the majority of the CO_2 emissions come from energy and heat production and transport. These sectors rely heavily on the combustion of (carbonaceous) fossil fuels, emitting large amounts of water vapour and carbon dioxide into the atmosphere as by-products. In attempts to combat these emissions, numerous governments around the world have taken action, ranging from the employment increasingly stringent CO_2 regulations to the promotion of sustainable alternatives, such as solar and wind energy.

Another important alternative that has gained popularity in more recent years is the use of hydrogen as an energy carrier. The combustion of hydrogen gives off only water vapours and a small amount of nitrous oxides, making it a suitable replacement for carbonaceous fuels from an emissions point of view. Additionally, hydrogen can be produced through electrolysis, converted back into electricity by means of a fuel cell and storing hydrogen is much easier than storing electricity. These attributes fit in nicely with the electrification trend of recent years [7].

1.1. Problem analysis

The transition to hydrogen as a fuel in combustion engines is not as straightforward as it might seem. Due to the wildly different molecular and combustion properties of hydrogen, it cannot simply be swapped out for natural gas or gasoline. Looking at the combustion process in particular, the two main problems are the low volumetric energy content of hydrogen and its combustion characteristics.

Property		**Hydrogen**	**Methane**
Molecular weight	(g/mole)	2.016	16.043
Normal boiling point	(K)	20	111
Liquid density @ NBP	(g/l)	71	422
Enthalpy of vaporization	(kJ/mole)	0.92	8.5
Lower Heating Value	(MJ/kg)	119.96	50.02
Flammability limits in air	(vol%)	4 - 75	5.3 - 15
Explosive limits in air	(vol%)	18.3 - 59.0	6.3 - 13.5
Spontaneous ignition pressure	(bar)	41	100
Stoichiometric volume ratio in air	(-)	2.39	9.48
Ignition energy	(J)	0.02	0.29
Adiabatic flame temperature in air	(K)	2318	2148
Autoignition temperature	(K)	858	813
Burning velocity in air	(m/s)	2.6 - 3.2	0.37 - 0.45
Diffusivity in air	(cm^2/s)	0.63	0.2

Table 1.1: Comparison of the properties of hydrogen and methane [1]

As can be seen in table 1.1, the volumetric energy density of hydrogen is much lower than that of methane (or other hydrocarbon fuels for that matter), while its stoichiometric ratio is higher. This requires hydrogen combustion engines to be much larger than their hydrocarbon fueled counterparts for a given power output. The combustion properties of hydrogen, especially the diffusivity and flame speed, are both a blessing and a curse. The high diffusivity of hydrogen promotes homogeneous air-fuel mixtures while the high flame speed increases combustion efficiency. On the other hand does this combination of properties pose a serious risk of flashback in open cycle engines such as gas turbines.

Gas turbines typically operate at very lean air-fuel mixtures. To sustain stable combustion however, the fuel is burned rich in the primary combustion zone, with additional air being added later on for complete combustion. Figure 1.2 shows (a part of) the combustor and the gas flows within. The outer recirculation zone contains a lot of hot, unburned fuel. Normally, when additional air enters through the walls of the combustion chamber, it reacts with the hot fuel mixture inside the combustion chamber. Keeping the air velocity at a higher value than the flame velocity makes sure that the flame cannot propagate upstream, preventing

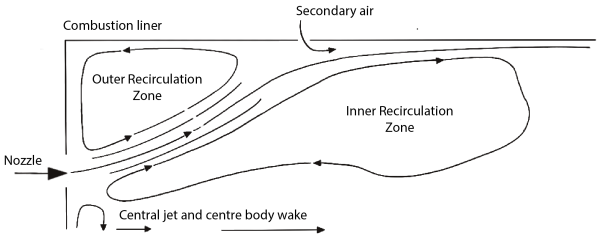

Figure 1.2: The flows inside a gas turbine combustor.

flashbacks. Hydrogen, however, has such a high diffusivity that it can diffuse upstream of the combustion chamber, towards the compressor. Moreover, the flame speed of hydrogen is nearly ten times higher than that of methane, making it nearly impossible to guarantee a high enough air velocity. These combined properties make hydrogen flashback a serious risk[54].

Flashback mechanics have been studied extensively since the 1940's and a general understanding of the underlying mechanisms have achieved. In a gas turbine combustion chamber, flashback can occur via four different mechanisms: core flow flashback, combustion instability induced flashback, combustion induced vortex breakdown and lastly boundary layer flashback[52]. Core flow flashback can occur when the turbulent flame velocity is greater than the bulk flow velocity. Combustion instability induced flashback can occur when the fluctuations generated by combustion accoustics are so great that they disrupt the local flow structure and generate large vortices leading to flow reversal. Combustion induced vortex breakdown is seen only in swirl stabilized gas turbine combustors, where the stabilizing vortex breaks down due to abrupt changes in the azimuthal velocity due to combustion. Consequently, recirculation zones can form that allow for flashback. The last mechanism, boundary layer flashback, is the main mechanism by which flashback can occur in jet flames. Generally, the bulk velocity is far higher than the turbulent flame velocity under normal operating conditions and flashback cannot occur in the core flow. Close to the walls however, the flow velocity is greatly reduced because of the imposed no slip boundary condition. The burning velocity also decreases closer to the wall and completely extinguishes in the "quenching zone" due to flame stretching and wall quenching effects. There exists a region in the boundary layer between the bulk flow and the quenching zone where flashback can occur. These circumstances are characterized by the critical velocity gradient, a function of the viscosity (μ_u) and the amount of shear stress (τ_w) in the fluid (figure 1.3 and equation 1.1)[53].

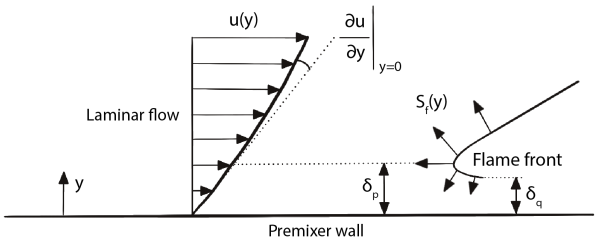

Figure 1.3: Critical velocity gradient schematic.

$$g = \frac{\partial u}{\partial y} = \frac{\tau_w}{\mu_u} \tag{1.1}$$

The critical velocity gradient model is a simple approximation of the flow in the boundary layer where combustion is assumed to not disturb the flow. Here, $u(y)$ denotes the velocity profile of the unburnt mixture, which is assumed to be laminar. $S_f(y)$ denotes the flame velocity and δ_q denotes the quenching distance. δ_p denotes the penetration distance, which is defined as the distance from the wall where the flame velocity is equal to the laminar flow velocity. This yields an expression for the critical velocity gradient (equation 1.2). Flashback can occur when $g > g_c$, or in other words when the flame velocity $S_f(y)$ is greater than the laminar flow velocity $u(y)$.

$$g_c = \frac{u(y = \delta_p)}{\delta_p} \tag{1.2}$$

The accuracy of this model greatly depends on the accuracy with which the penetration distance can be determined. Numerous studies have been conducted and good approximations have been found, however an exact relation between the penetration distance and the temperature, fuel composition, equivalence ratio and pressure has not yet been found.

To aid future research in determining flashback behaviour, it is paramount that these parameters can be measured with the greatest accuracy possible. The region of interest is small and close to the wall and the mere presence of a physical probe (such as a thermometry or flue gas probe) would significantly perturb the local temperature and flow field. Ex situ measurement techniques such as Laser Induced FLuorescence (LIF) can be used to determine species concentrations without affecting the temperature and flow field. However, this technique is not suitable for hydrogen. OH chemiluminescence can be utilized to derive the presence of hydrogen, but this relies on the oxidation of hydrogen in the first place. To be able to simultaneously measure temperature, pressure and relative species concentration non-intrusively, a technique such as Coherent Anti-Stokes Raman Spectroscopy (CARS) is required. CARS is a form of laser diagnostics often used in combustion research because of the capabilities to perform in situ gas phase measurements at high temperatures and pressures, as well as relative species concentrations with high accuracy. This technique has already been successfully been employed to perform multi-species measurements flame-wall interactions[42].

1.2. Research goal

The previous chapter touched upon one of the many challenges concerning the use of hydrogen as a fuel. It is not the aim of this research to solve this problem, in part because there are few tools to do so. Instead, this research looks to a specific measurement technique to further develop existing tools for measuring and predicting the presence of hydrogen molecules and their temperature. Succeeding here will aid in determining hydrogen flashback conditions in gas turbine combustors, as specified earlier.

To get the best result possible, the measurements will have to be done in situ. Preferably, these measurements would also be non-intrusive as to not disturb the flow, temperature and chemical characteristics. Lastly, in order to capture the highly turbulent character of the flow inside a combustor, the repetition rate of the tool should be high enough to capture its behaviour. A suitable candidate for such a measurement tool is called Coherent Anti-Stokes Raman Spectroscopy (CARS). It utilizes a number of laser beams focused at the point of interest to generate a signal that contains accurate information about the species present at the moment of measuring, as well as its temperature. Additionally, the molecules always return to their ground state after being hit by the laser beams, leaving their internal energy unchanged. The setup used in this research can carry out independent measurements at a frequency of 1kHz, but other setups exist that go well beyond that. This allows for accurate measurements even in highly turbulent environments.

A successful CARS measurement yields a unique molecular response that can be Fourier transformed to obtain the Raman shift versus intensity. To obtain parameters such as temperature, the measurement data has to be compared with a valid model. When the measurement data and model prediction comply, the inputs of the model can be taken to be the actual values at the point of measuring. Models for predicting the molecular response of hydrogen are scarce due to the difficulty of both measuring and modelling the response of hydrogen. The laser energy required to adequately excite hydrogen is very high and the molecular constant needed for the model are hard to obtain and do not display any sort of scaling behaviour.

Researchers at the AWEP department of the Delft University of Technology have built a CARS setup and have used it to successfully characterize the Raman spectra of N_2 and O_2 and are now looking to do the same for H_2. With that, the main research question is: **Can the current two-beam hybrid fs/ps CARS setup be used to perform accurate thermometry on hydrogen alone?** There are three different aspects of the problem that need to be addressed in order to answer this question:

- **What is the feasibility of probing hydrogen using the standard 35 fs pulse of the regenerative amplifier?** The peaks in the hydrogen spectrum are much further apart in the frequency domain compared to nitrogen and oxygen, so a larger excitation bandwidth is required to capture the entire spectrum. The larger the part of the spectrum that can be captured, the more accurately the temperature can be evaluated. Evaluating just a few peaks may affect the precision and accuracy of the measurements.

- **What is the feasibility of simultaneously measuring nitrogen and hydrogen for benchmarking purposes?** When gathering multi-species data, the evaluated temperature for both species should be the same, allowing for calibration and validation. However, because the local temperature can fluctuate a lot, the data must be gathered simultaneously to ensure the measurement data was taken at the same temperature. This poses challenges for both the spectral range and resolution of the measurements as well as the relative signal intensity.

- **What is the feasibility of utilizing a compressed 10 fs pulse to probe hydrogen?** Because of the limited available bandwidth of the standard pulse, it is not possible to record the entire spectrum corresponding to the molecular response of hydrogen. The pulse can however be compressed to 10 fs through filamentation, but this might incur stability issues and inaccuracies at higher Raman shifts.

1.3. History of CARS

Since the first observance of three wave mixing by Maker and Terhune in 1965, and the first applications of CARS in the 1970's, the technique has been under constant development and is considered by many to be the best tool for measuring gas phase thermometry and relative species concentrations, especially in combusting flows. Combustion environments often prove troublesome for conventional temperature measurement tools, because of various heat transfer phenomena. CARS on the other hand, is used specifically for this purpose because it directly measures the temperature dependent Boltzmann population distribution of the rotational and vibrational energy states of a molecule. Each molecule has its own unique spectral structure, allowing for recognition of different species. Absolute concentrations can not (yet) be measured with this technique, but the relative intensity of the spectral structures gives information on the relative concentrations of the species. Most commonly, this is done with respect to nitrogen, because it is usually inert, well understood, and available in both the products and reactants side in most practical combustion environments.

Initially, CARS was done on a nanosecond scale. Nanosecond laser sources had to be used to supply sufficient energy in order to drive the third order nonlinear processes on which CARS is dependent. For a long time, Nd:YAG lasers were used in various arrangements because of their high pulse energy and their compatibility with laser dyes. These lasers had some significant drawbacks however. The repetition rate of the pulses was typically no higher than 20 Hz and on the nanosecond timescale, the molecules undergo countless collisions. Due to the high pulse energy in nanosecond CARS, detailed spectral information can be obtained, but the information is not time resolved. Additionally, the relatively long nanosecond pulses of the pump, Stokes and probe lasers overlap, giving rise to a significant non-resonant contribution to the signal. The molecular collisions severely affect the linewidths of the measured spectral structures, leading to line mixing and convolution of the spectrum. The nonresonant signal obscures the resonant signal, making signal analysis harder. At the time, the non-resonant contribution could be suppressed through a polarization approach, but not without also cutting into the resonant signal.

In the 1980's, picosecond CARS was utilized for the first time, offering temporal resolution at the cost of some spectral resolution. In addition, picosecond CARS could be used to suppress the non-resonant signal by separating the pump and probe pulses in the time domain. The lower pulse duration also meant that fewer collisions would occur during probing. Picosecond CARS allowed the investigation of how the molecular transitions decay with time and what their influences on the perceived temperature and concentration are. In the 2000's, femtosecond CARS was introduced. The high bandwidth that comes with these ultra short pulses required the signals to be analyzed in the time domain, instead of the frequency domain. The broad excitation bandwidth allowed excitation of multiple species at the same time and femtosecond CARS was used to achieve kHz repetition rates for the first time.

The most recent developments in the field of CARS have been on hybrid femtosecond/picosecond CARS. This type of CARS combines the best of both worlds, the wide excitation bandwidth and high repetition rates of the fs pulses with the spectral resolution and non-resonant background suppression of the ps probe. Joseph Daniel Miller did important work in this area by evaluating the feasibility of such an approach, which he published in his doctoral thesis in 2012. He demonstrated the use of hybrid fs/ps CARS for quantitative temperature measurements in heated flows for molecular hydrogen, nitrogen and oxygen. He achieved better than 3% accuracy in 1 kHz single shot high temperature (1400-2400 K) measurements in hydrogen, and even better than 1.5% in low temperature (300-700 K) hydrogen. A year later, Alexis Bohlin, Brian Patterson and Christo-

pher Kliewer successfully employed a two beam hybrid CARS setup and the corresponding phase matching criteria. Their setup significantly simplified phase matching criteria as compared to three beam CARS and achieved a much greater robustness, ultimately leading to higher signal levels. Additionally, line imaging was achieved using this setup and there is even the possibility of performing 2-D CARS thermometry[40]. Another year later, in 2014, Sean Kearney presented a very detailed and critical assessment of hybrid rotational CARS thermometry over a wide range of flame conditions and different types of fuel, showing the combined robustness and accuracy of the technique[44]. In 2017, Trevor Courtney, Alexis Bohlin, Brian Patterson and Christopher Kliewer employed ultra broadband pump/Stokes pulses to extend the excitation bandwidth to 0-2200 wavenumbers[38]. This allowed for the detection of the pure rotational hydrogen S-branch and evaluate its feasibility for thermometry, achieving a 5% accuracy on average over a 300-1600 K range. The research presented in this thesis will build on these discoveries.

2

Coherent Anti-Stokes Raman Spectroscopy

The main measurement technique used in this research is Coherent Anti-Stokes Raman Spectroscopy, or CARS. It is a technique based on the nonlinear conversion of two or more electric fields originating from laser beams into a coherent laser-like Raman signal, containing species and temperature specific information about the probed location. Since its discovery in 1965, CARS has been continually improved and developed to the point where it has become the most accurate method of performing gas phase thermometry. Additionally, the capabilities of discerning various species is varying concentrations in conjunction with their temperature, even at high pressures, makes CARS a very powerful tool indeed. A description of how CARS works is given in the paragraphs below.

2.1. CARS process

CARS is a non-linear four wave mixing process in which three different electric fields originating from a pump, probe and Stokes photon interact with a Raman active medium to produce a fourth electric field, belonging to the CARS signal photon[37],[49]. The energy level diagram corresponding to this process is shown in figure 2.1. The pump and the Stokes photons excite the molecule from its ground state to a resonant energy state where the energy difference between the pump and Stokes photons is equal to the energy difference between the ground state and the resonant state. These resonant states can correspond to rotational, vibrational or electronic energy states. The probe then inelastically scatters off the molecules in these resonant states. As a result, the molecule falls back to its ground state and the probe photon (now the anti-Stokes photon) experiences a shift in frequency. This frequency shift corresponds to the energy difference between the ground state and the excited state of the molecule, therefore carrying information about the resonant state it scattered off of. Since the probe is a narrowband laser with a known frequency, measuring the Raman shift of the anti-Stokes photon thus enables determining what molecule and in which state it scattered from.

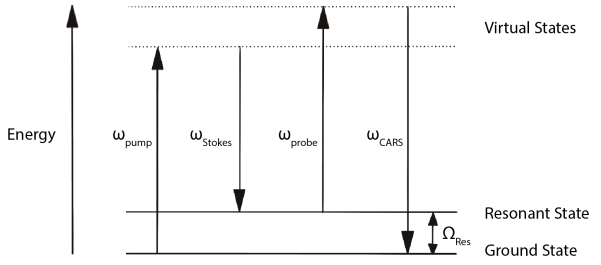

Figure 2.1: Energy level diagram of the CARS process.

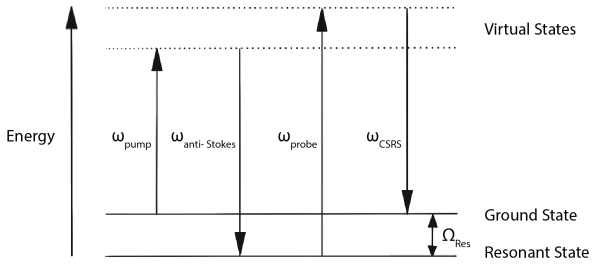

Figure 2.2: Energy level diagram of the CSRS process.

Analogous to the CARS process there is the CSRS process, depicted in figure 2.2. The CARS process excites the molecules to a higher energy state, resulting in a CARS signal that is blue-shifted relative to the probe. The CSRS process excites the molecule to lower energy states, resulting in a CSRS signal that is red-shifted relative to the probe. When a molecule is excited, both these processes happen simultaneously.

2.2. Resonant transitions

The photon energy difference absorbed by the molecule causes a transition in the molecule. As long as there is sufficient bandwidth, all transitions are excited simultaneously. In theory it would be possible to observe the entire range of the signal if the sensor is large enough. In practice however, this means limiting to a certain region of interest, or "branch" of the signal. Transitions can occur between different vibrational levels and different rotational levels, where the energy difference between two vibrational levels is large compared to the energy difference between two rotational levels. For a given vibrational transition, many different rotational transitions occur whose Raman shifted signals are spectrally close together.

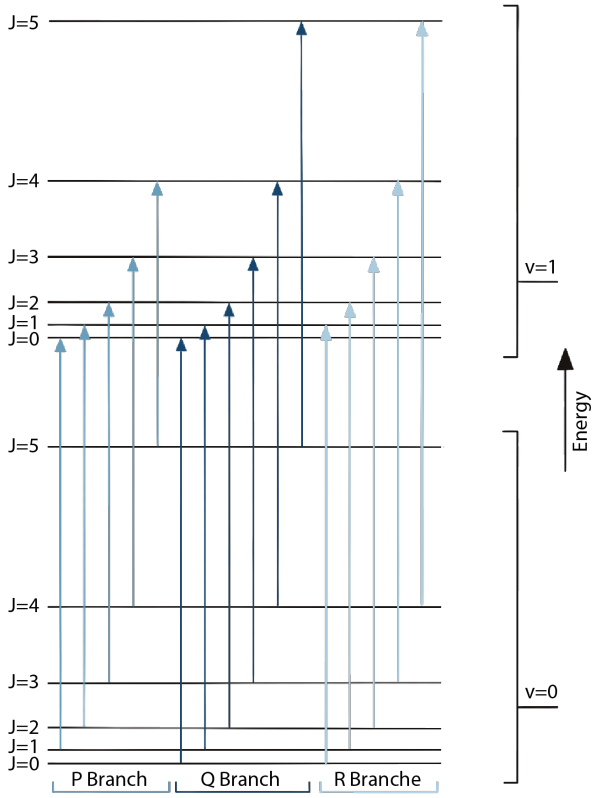

Figure 2.3: Transitions for the rovibrational P- and R-branches and pure vibrational Q-branch.

The collection of signals from the different rotational transitions within a vibrational transition are called branches. Figure 2.3 shows a number of transitions within a few different branches. The length of the arrows represent the required energy for such a transition. Selection rules apply for each type of branch of a certain molecule, given in table 2.1. Here Δv gives the difference in vibrational levels and ΔJ the difference in rotational levels. In this research, the pure rotational S-branch of hydrogen is investigated.

Transition	Δv	ΔJ	Branch
Pure rotational	0	-2	O
Pure vibrational	1	0	Q
Pure rotational	0	+2	S
Rovibrational	≥ 1	-2	O
Rovibrational	≥ 1	+2	S

Table 2.1: Selection rules for different energy transitions in linear molecules.

2.3. Hybrid femtosecond/picosecond CARS

This research makes use of a hybrid femtosecond/picosecond CARS arrangement, referring to pulse duration of the beams involved. A schematic of hybrid fs/ps CARS in the time domain is shown in figure 2.4.

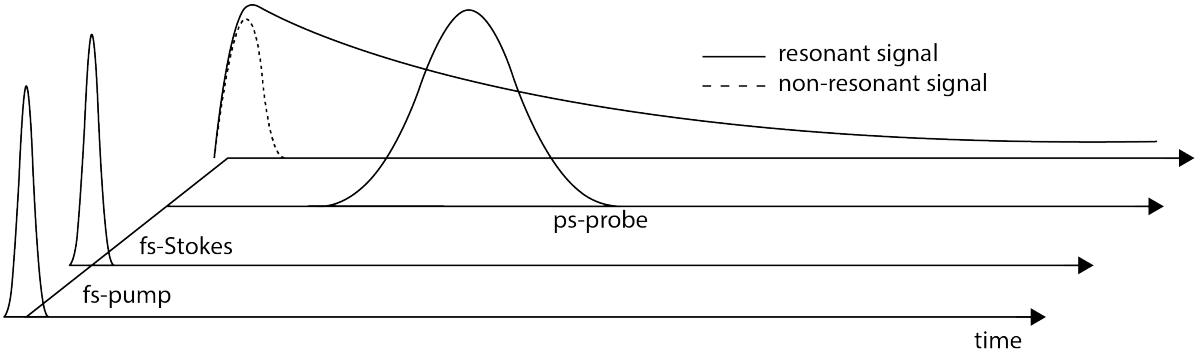

Figure 2.4: The hybrid fs/ps CARS process in the time domain.

The pump/Stokes beam has a pulse duration in the order of around 35 femtosecond, while the probe pulse has a pulse duration that can be tuned to be between 4 and 15 picoseconds. The pump and Stokes photons arrive simultaneously, after which they excite resonant and non-resonant transitions. The non-resonant transitions die down quickly, but the resonant states have a much longer lifetime. The picosecond probe then scatters from these resonant states. On a picosecond timescale, this process can be assumed collisionally independent. This means the excited molecules have no time to transfer their energy during the probing period, which would otherwise result in line broadening. This is in contrast to nanosecond CARS setups that have been used a lot in the past. The low pulse duration in the femtosecond beam implies a large spectral bandwidth in the case of (near) transform limited pulses. The picosecond probe is long enough to still be considered narrowband, but short enough not to overlap with the pump/Stokes beam. The major advantage of this, in stark contrast to nanosecond CARS, is that the generation of non-resonant signals is nearly nonexistent.

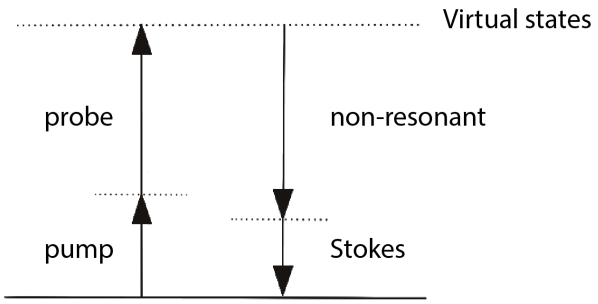

Figure 2.5: An energy level diagram depicting non-resonant four wave mixing.

If the pump/Stokes and probe pulses were to overlap in time, probe photons can much more easily scatter from the non-resonant states. Because these photons were not scattered from a resonant state, they contain no information about temperature or species concentration. The resonant and non-resonant signals overlap in the frequency domain, obscuring the resonant contribution and making it harder to find a good fit for the data.

2.4. Induced polarization

All optical effects (linear and non-linear) are the result of interaction between the electric field component of light (as electromagnetic radiation) and the charged particles in the corresponding material. The electric field component of visible light has a frequency of around 10^3 THz. These oscillations are so fast that only particles as light as electrons can follow them adiabatically. The position of the nuclei remains unaffected by such an electric field, while the electrons are continually slightly displaced from their equilibrium positions. This induces a time dependent dipole moment according to equation 2.1. The dipole moment μ is the result of the displacement $r(t)$ and the charge e of the electron[23].

$$\mu(t) = -e \cdot r(t) \tag{2.1}$$

The macroscopic polarization is equal to the sum of all individual dipole moments and in the limit of weak electric fields the electron displacement scales linearly with the applied electric field strength. This results in equation 2.2. Here χ is the material susceptibility and ϵ is the electric permittivity in vacuum.

$$P(t) = N\mu(t) = \epsilon_0 \chi E(t) \tag{2.2}$$

For stronger electric fields however, the electrons are displaced beyond their harmonic linear response and resulting motion cannot be described by linear equations. In other words, the response is non-linear. If the anharmonic contributions to the motion of the electron are small, the behaviour can be approximated rather well by using a power series. Such an equation is given in equation 2.3[50].

$$P(t) = P^1(t) + P^2(t) + P^3(t) + ... = \epsilon_0 \left[\chi^{(1)} E(t) + \chi^{(2)} E^2(t) + \chi^{(3)} E^3(t) + ... \right] \tag{2.3}$$

In isotropic materials (like gases), all even order terms cancel out due to inversion symmetry in the material. This leaves the third order polarisation $P^3(t) = \chi^{(3)} E^3(t)$ as the lowest non-linear order and therefore the strongest contributor to the non-linear polarization in CARS. The basis of this effect lies in quantum mechanics and an exact formulation for the third order polarisation can be derived from combining the Schrödinger equation with the density matrix and classical electromagnetic optical wave theory. Excellent derivations of this can be found in literature. Equation 2.4 shows an expression for the third order polarization valid for hybrid fs/ps CARS.

$$P^{(3)}(t) = \left(-\frac{i}{\hbar} \right)^3 \cdot E_3(t-\tau) \cdot R_4(t) \cdot e^{-i\omega_3(t-\tau)} \tag{2.4}$$

2.5. Molecular response function

$R_4(t)$ in euqation 2.4 is called the third order non-linear response function, also known as the molecular response, which describes the behaviour of the molecule in the time domain after excitation by the pump/Stokes beams. A general expression of this response is given by equation 2.5[51].

$$R_4(t) = \sum_{m,n} I_{m,n} \times e^{\left[\frac{t}{\hbar} \left(i\Delta E_{m,n} - \frac{\Gamma_{m,n}}{2} \right) \right]} \tag{2.5}$$

Here, m and n denote the initial and final state, each having a certain vibrational and rotational energy level. In the general form, this equation describes the molecular response as the sum over all Raman active transitions. However, in this research only the pure rotational S-branch transitions are evaluated, which are all transitions that have unchanged vibrational levels while the rotational level increases by 2. Another way of writing this is through the selection rules $\Delta J = +2$ and $\Delta v = 0$. The form of equation 2.5 specific to the pure rotational S-branch now becomes equation 2.6.

$$R_4(t) = \sum_{v} \sum_{J} I_{v,J;v,J+2} \times e^{\left[\frac{t}{\hbar} \left(i\Delta E_{v,J;v,J+2} - \frac{\Gamma^S_{v,J;v,J+2}}{2} \right) \right]} \tag{2.6}$$

The equation now describes the molecular response of an arbitrary S-branch transition summed over all possible rotational and vibrational levels. The molecular response can be broken down into three main distinguishing features and their influences: $I_{v,J;v,J+2}$ dictates the transition strength, $E_{v,J;v,J+2}$ the transition frequency and finally $\Gamma^S_{v,J;v,J+2}$ the transition linewidth. These features are more easily explained when considering a the molecular response of a single transition, such as the one in figure **??**.

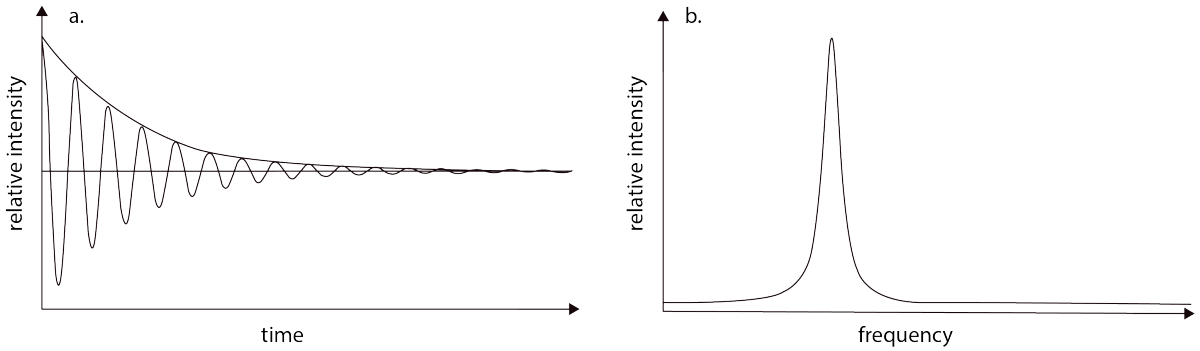

Figure 2.6: The molecular response of a single transition in the a. time and b. frequency domain.

In the time domain, the molecular response looks like a decaying sinusoidal wave. The frequency of oscillation is determined by the transition frequency and the rate of (exponential) decay is determined by the transition line width. A Fourier transform of the solution transform it to the frequency domain, shown on the right in figure 2.6. Here, transition line strength corresponds to the height of the peak, the transition frequency corresponds to the location of the peak and the transition line width corresponds to the width of the peak. Considering the frequency domain is especially useful when the molecular response of an ensemble of transitions is calculated, demonstrated in figure 2.7.

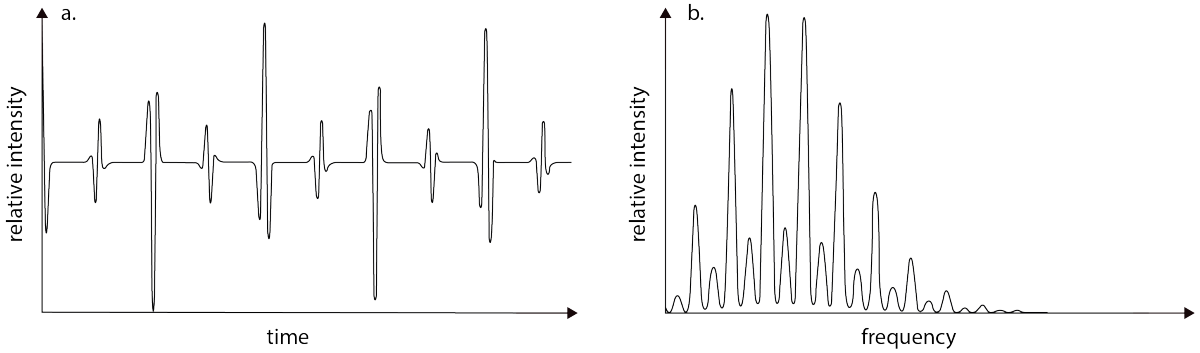

Figure 2.7: The molecular response of an ensemble of S-branch transitions in the a. time and b. frequency domain.

The time domain signal is now a large sum of decaying sine waves, each with a different frequency, rate of decay and intensity. In the frequency domain, each of these transitions is again characterized by a peak. Because the transition line strength, transition frequency and transition line width all depend on unique molecular constants, evaluating the molecular response allows for identification of the molecule it originated from.

3

Theoretical model

The third-order nonlinear susceptibility discussed earlier can be modelled in the time domain according to the equation below. It is assumed that the signal is the sum of elementary sine waves at the frequency of each individual Raman transition. These transition are weighted by their relative probability of occurring. Here, J+2 denotes the S-branch transition.

$$\chi^{(3)}(t) = \sum_{k}\sum_{v}\sum_{\Delta J=+2} X_k \gamma_k^2 F^{(k)}_{J\rightarrow J+2} b_{J\rightarrow J+2}\left(N^{(k)}_{J+2} - N^{(k)}_{J}\right) exp\left[\left(i\omega^{(k)}_{v,J\rightarrow J+2} - \Gamma^{(k)}_{J\rightarrow J+2}\right)t\right] \tag{3.1}$$

The third-order susceptibility depends on the mole fraction of the species ($X_(k)$), the polarisation anisotropy (γ_k), and the population density of the various energy levels ($N^{(k)}_{J+2} - N^{(k)}_{J}$). This is the corrected for rovibrational coupling and branch transition probability by the Herman-Wallis factor ($F^{(k)}_{J\rightarrow J+2}$) and Placzek-Teller coefficient ($b_{J\rightarrow J+2}$). It is then multiplied by the exponent of the imaginary part of the Raman frequencies for rotational transitions ($i\omega^{(k)}_{v,J\rightarrow J+2}(t)$), introducing the sine waves. The exponent of the measured linewidths is then subtracted ($\Gamma^{(k)}_{J\rightarrow J+2}(t)$), introducing natural decay (damping) into the model. Finally, this equation is summed over all possible rotational and vibrational states, and all possible species to get a complete signal.

One of the main goals of this research is to implement an existing theoretical model that can accurately predict the molecular response. The experiments produce a certain data set that will have to be evaluated by comparing it to the model data. The model is used to generate thousands of data sets for all combinations of input parameters. The experimental data is then compared against all possible model data sets, and are evaluated through taking the root sum squared. A minimum value of this sum indicates the best fit between the experimental data and the model prediction. The input parameters corresponding to the best model fit are then said to also be the values in the experimental data. To be able to properly interpret the model, one should understand how both the model and the molecule behave and where discrepancies could arise. To model spectrum corresponding to the molecular response, there are three main components that need to be taken into account: the line positions, the line strength and the line width. In a nutshell, the line positions allows differentiation between species and the line strength allows determination of temperature and relative concentration. The next few sections each explain a different part of the code to give a better understanding of how it works.

3.1. Line position

The line positions in a spectrum are the Raman shifted frequencies determined by the energy levels of the populated rotational and vibrational states for a given molecule. The frequency at which a line is centered equates to the energy that is required to excite the molecule to the corresponding energy level. This energy level depends in part on the rotational and vibrational states that are populated (higher states have higher energies) but also on molecule specific constants. These molecular constants dictate how much the lines are spaced in a spectrum and they are the reason that different molecules each have their own distinct spectrum.

3.1.1. Rigid rotor model

In order to understand how light matter interaction works, it is important to get a feel for molecular dynamics. Molecular dynamics can get extremely complicated very quickly depending on the molecule's size, but is luckily reasonably manageable for diatomic molecules such as hydrogen. A hydrogen molecule is essentially two hydrogen atoms bound together. The bond acts as a spring, and the hydrogen atoms are free to vibrate. Besides vibration, the molecule can also rotate as a whole along the three primary axes. As the molecule rotates, the centrifugal force affects the vibration mode. Conversely, the unrelenting vibration means that the molecule's moment of inertia is constantly changing, in turn constantly affecting the speed of rotation if the molecule remains otherwise unperturbed. To complicate things even further, consider that each hydrogen atom consists of a positive nucleus with a negative orbiting electron. The atomic nucleus-electron pair is in itself another rotor system, but the orbiting electrons exert varying repelling forces on one another and the (positive) nuclei exert varying attractive forces on the orbiting electron of the other nucleus. Even the dynamics of a molecule as "simple" as hydrogen are far too complicated to solve analytically. Needless to say, simplifications need to be made.

A popular model often used for studying diatomic molecules is the rigid rotor model (figure 3.1). This model radically simplifies the dynamics of diatomic molecules by assuming they can be modelled as two point masses bonded over a fixed distance. This means that the individual atoms can no longer vibrate, but can only rotate as a whole. Because of the assumption that the atoms can be modelled as point masses, the moment of inertia along the bond axis is always zero. Because of symmetry, the moments of inertia along the other two primary axes are both always nonzero and equal.

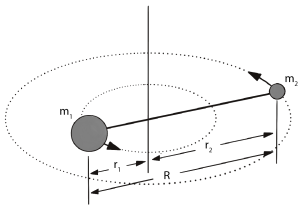

Figure 3.1: Rigid rotor model of a diatomic molecule [20].

The amount of energy a rigid rotor can have can easily be defined as a function of its moment of inertia and angular frequency and is given is equation 3.2.

$$E = 2\pi^2 \nu^2 I_B \tag{3.2}$$

However, this expression implies a continuous energy spectrum, impossible in quantum systems. In order to find the allowed discrete energies of such a systems, the Schrödinger wave equation will have to be solved for E. This yields an expression for the possible rotational energy levels as a function of the rotational quantum number J. This expression is given below [15]. The total derivation can easily be found in numerous books, lectures or online [16].

$$E = \frac{h^2 J(J+1)}{8\pi^2 I_B} = BJ(J+1) \tag{3.3}$$

The rigid rotor model works well, because the mass ratio of nuclei and electrons is approximately 1000 for hydrogen and even higher for other atoms. Also, the electromagnetic forces that individual particles exert on one another are weak. Generally speaking, a diatomic molecule vibrates about 1000 times for every rotation it completes. The difference in magnitude of energy of these motions means that it is justified to superimpose the rotational energies on the vibrational energies, according to the Born-Oppenheimer approximation [18]. The rigid rotor model is adequate when the vibrational energy is low and the robivrational coupling is negligible. When either vibrational or coupling effects need to be taken into account, additional models can be applied.

3.1.2. Anharmonic potential

In the case where decoupled vibrational energy also needs to be taken into account, the harmonic oscillator model can be used. This model assumes the diatomic molecule to be two point masses that are connected

with a spring. Because the vibrational and rotational motion are now decoupled, the harmonic oscillator and rigid rotor models can easily be superimposed.

Analogous to the approach for the rigid rotor model, an expression can be found for the discrete vibrational energies that a molecule can have. Equation 3.4 gives the expression of the first order vibrational energy levels as a function of the quantized vibrational state v and frequency v_{osc} [15]. The $\frac{1}{2}$ constant in the equation denotes the systems zero-point energy, the absolute minimum energy of a quantum-mechanical system (another consequence of the uncertainty principle).

$$E = h\upsilon_{osc}\left(\upsilon + \frac{1}{2}\right) \tag{3.4}$$

The harmonic oscillator model takes vibration into account, but does not consider the physical limits of this oscillation. There is both an upper and lower limit to how far the atoms can move from one another. The atoms cannot move too close together or they would touch and they cannot move too far apart or their bond would dissociate. This changes the potential energy surface of the harmonic oscillator. Figure 3.2 shows the harmonic oscillator potential energy curve and the Morse potential. The expression for the Morse potential can be found in equation 3.5

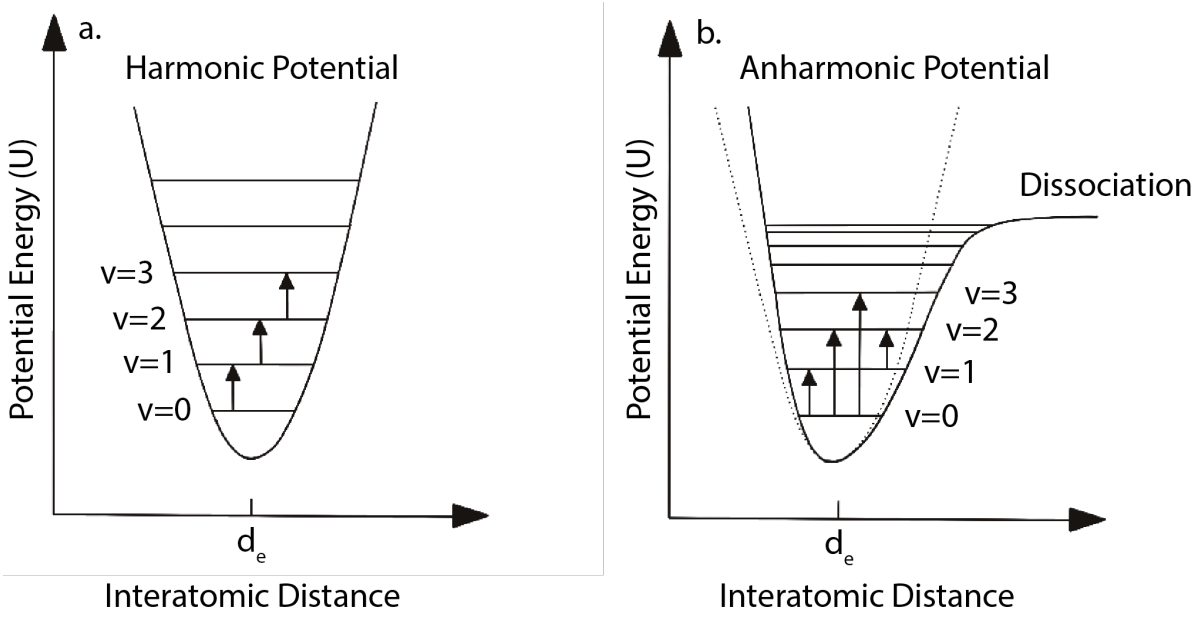

Figure 3.2: The difference in potential energy of the a. harmonic oscillator and b. the Morse potential.

$$U(d) = D_e\left(1 - e^{-\beta(d-d_e)}\right)^2 \tag{3.5}$$

The Morse potential is not an exact expression of the potential energy surface, however. The model is used for its simplicity as it relies on only three fitting parameters: β (defines the width of the well), D_e (depth of the well), and d_e (equilibrium distance between atoms) [19].. A more accurate representation can be obtained by using a Taylor expansion from the equilibrium separation distance. For most applications, a third order expansion suffices. As the figure clearly indicates, the upper and lower bounds of the harmonic potential are slightly shifted to the left, effectively elongating the average bond length of the molecule. Applying the Schrödinger equation to the equation for the Morse potential, yields the expression for the anharmonic vibrational energy (equation 3.6).

$$E = h\upsilon_{osc}\left(\upsilon + \frac{1}{2}\right) - x_m h\upsilon_{osc}\left(\upsilon + \frac{1}{2}\right)^2 \tag{3.6}$$

Equation 3.6 differs from equation 3.4 only in the second part, which is the anharmonic correction obtained from the Morse potential. Here, x_m is the first anharmonicity constant. Higher order Taylor expansions will

yield additional anharmonicity terms. As is evident from both the equation and the anharmonic potential in figure 3.2, the anharmonic correction pulls the energy levels of higher vibrational states closer together.

3.1.3. Vibration-rotation interaction

From figure 3.2 it seems that for the harmonic oscillator, the vibrational energy levels are evenly spaced. This is verified mathematically in equation 3.7 [35]. The difference btween all vibrational levels is constant.

$$\Delta E(v) = h\nu_{osc}\left(v+1+\frac{1}{2}\right) - h\nu_{osc}\left(v+\frac{1}{2}\right) = h\nu_{osc} \tag{3.7}$$

The same can be done for the rotational levels. As can be seen from equation 3.8, the difference between the energy levels increases with increasing value for the rotational quantum number.

$$\Delta E(J) = B(J+1)(J+2) - BJ(J+1) = 2B(J+1) \tag{3.8}$$

For high values of the vibrational quantum number, it was seen that the anharmonic nature caused the average bond length to extend. This has consequences for the rotational energy levels: As the bond length increases, the moment of inertia increases with it, effectively lowering the required energy for the next rotational state according to equation 3.3. The degree of rotation-vibration interaction can be captured in additional terms in said equation and is shown in equation 3.9 [21]. A more detailed derivation of this term and higher order terms through manipulation of the Hamiltonian can be found in McNab's book [18].

$$E = BJ(J+1) - DJ^2(J+1)^2 \tag{3.9}$$

3.2. Line strength

The line strength in a spectrum is a measure of the amplitude of the different lines relative to each other. These can be used to determine the temperature and relative concentration of the species involved. Th next few paragraphs explains what effects have to be taken into account in order to get accurate results and how to calculate them

3.2.1. Boltzmann population distribution

The Boltzmann population distribution shows how much a certain rotational state is populated for a given molecule at a given temperature. The population difference between the initial state and the final state is directly proportional to the line strength of that transition. The Boltzmann population distribution is given in equation 3.10 and the population difference is given in equation 3.11, where the sum $Z_{v,J}$ is given in equation 3.12.

$$\rho_{v,J} = \frac{(2J+1)e^{-\frac{E_{v,J}}{k_B T}}}{Z_{v,J}} \tag{3.10}$$

$$\Delta\rho_{\Delta v=0,\Delta J=2} = \frac{g_J(2J+1)}{Z_{v,J}}\left[e^{-\frac{E_{v,J}}{k_B T}} - e^{-\frac{E_{v,J+2}}{k_B T}}\right] \tag{3.11}$$

$$Z_{v,J} = \sum_v \sum_J (2J+1)e^{-\frac{E_{v,J}}{k_B T}} \tag{3.12}$$

It is a normal Boltzmann distribution, with one exception; the odd and even J-states are not populated to the same degree. This can be seen in the figures below. This effect is due to spin degeneracy of the state of the molecule[**?**]. Two or more different states can have the same energy level, thus making that energy level more populated. For degenerate states at a certain energy level, all states are equally likely to occur.

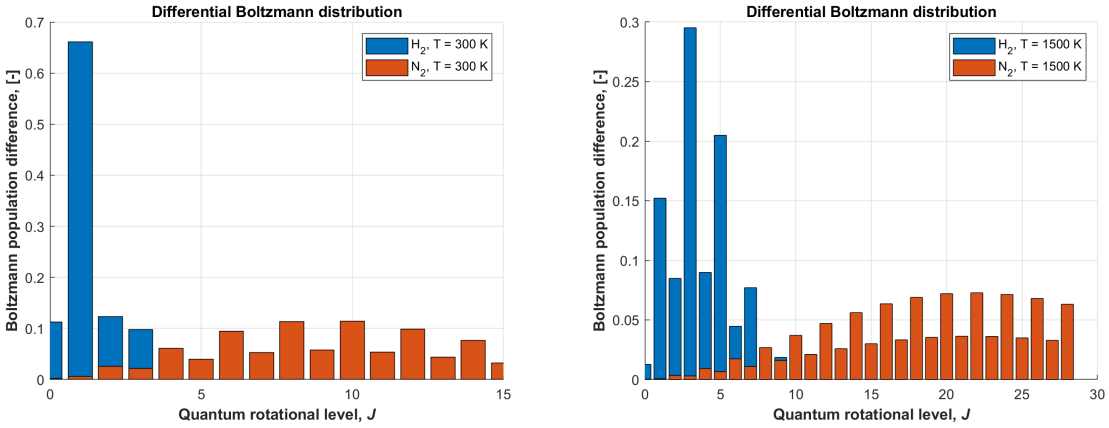

Figure 3.3: The Boltzmann population differences for H_2 and N_2 at 300 and 1500 K.

As can be seen from the figure above, hydrogen only populates a few rotational states, whereas nitrogen readily populates 60 rotational states at higher temperatures. This is due to the higher difference in energy between the rotational energy levels of hydrogen.

3.2.2. Placzek-Teller coefficient

The Placzek-Teller coefficients describe the effect of the rotation-vibration interaction in a molecule on the polarizability of the molecule, which affects the transition strengths. The relative transition strength of the O-, Q- and S-branch as a function of the rotational level is given by equations 3.2.2[8], and plotted in figure 3.4.

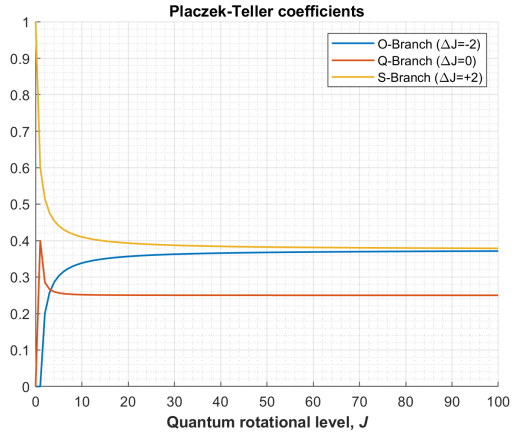

Figure 3.4: Placzek-Teller coefficients for the O-, Q-, and S-branch.

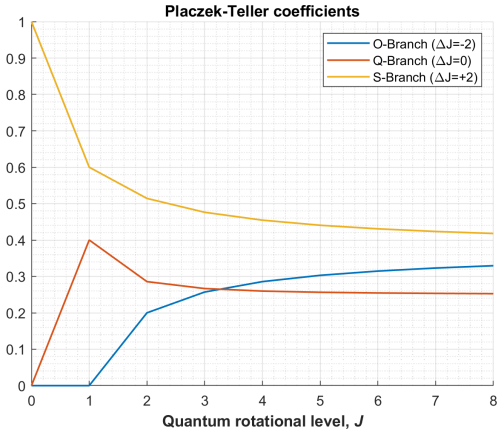

Figure 3.5: Placzek-Teller coefficients for the first few rotational levels.

$$P_O(J \to J-2) = \frac{3J(J-1)}{2(2J-1)(2J+1)} \tag{3.13}$$

$$P_Q(J \to J) = \frac{J(J+1)}{(2J-1)(2J+3)} \tag{3.14}$$

$$P_S(J \to J+2) = \frac{3(J+1)(J+2)}{2(2J+1)(2J+3)} \tag{3.15}$$

Some molecules, such as CO_2, have very small spacings between the rotational energy levels and therefore populate a lot of rotational states. For such molecules the influence of the Placzek-Teller coefficient is less important because in the limit the coefficients for the O-branch transitions (CSRS side) and S-branch transitions (CARS side) equalize, giving approximately equal signals for both sides. The Placzek-Teller coefficients

are especially important for hydrogen, because its rotation-vibration interaction is extremely strong. Because the spacings between the rotational energy levels in hydrogen are so high, hydrogen never populates more than a handful of rotational levels, making the influence of the Placzek-Teller coefficients significant even at elevated temperatures. Figure 3.5 shows the Placzek-Teller coefficients in greater detail for the first few rotational levels. As can be seen from the figure, no signal is expected whatsoever for the first two O-branch transitions, and remains very low for the few transitions thereafter. This is the reason why for hydrogen, the signals are observed at the CARS side (S-branch).

3.2.3. Herman-Wallis factor

The Herman–Wallis factor is a molecular parameter that measures the influence of centrifugal force on the polarizability of the molecule, and therefore on the intensity of the spectral lines [9]. This effect is larger for very light molecules, because their rovibrational coupling is stronger. There are a number of different approaches to determine these factors, resulting in different models and calculations. In a recent paper by Courtney et al[38] on the ultra broadband excitation of the pure rotational hydrogen S-branch, the Herman-Wallis factors by Tipping and Ogilvie were used. The justification for this choice is extensively elaborated on in a paper by Bohlin et al[46], where different Herman-Wallis factors are compared. Due to the good thermometric accuracy achieved in these papers and similarities in the type of research this is therefore also the model used in this thesis. The expression is given in equation 3.16.

$$F(J) = \left[1 + \left(\frac{2B_e}{\omega_e}\right)^2 \cdot (J^2 + 3J + 3)\frac{r_e \cdot d\beta_e}{\beta_e}\right]^2 \tag{3.16}$$

Figure 3.6 shows two different versions of the Herman-Wallis factors for both hydrogen and nitrogen. As can be seen, the effect of the Herman-Wallis factors is significant for hydrogen even at low rotational levels, whereas a molecule with weak rovibrational like nitrogen coupling is barely affected. It also shows the importance of selecting the right model for the Herman-Wallis factors for a particular application, as selecting the wrong model can have a significant impact.

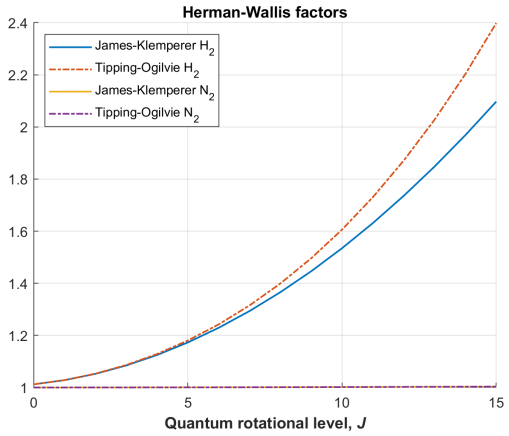

Figure 3.6: Two different Herman-Wallis factors for hydrogen and nitrogen.

3.2.4. Excitation efficiency

Excitation of the molecules happens through the combined absorption and emission of photons by the pump/Stokes laser combination. The difference in photon frequency is equal to the energy that excites the molecule. If the bandwidth is infinite, all possible combination of photon pairs are equally likely to occur. However, the laser bandwidth is limited. This means that the greatest difference in photon energy (and thus greatest possible excitation energy) depends on the available photons at each end of the available bandwidth. This also means that the higher the energy difference of the photon pairs, the fewer possible configurations there are to find these pairs in the given bandwidth. This translates to lower rotational states being excited more frequently or efficiently than higher rotational states.

This excitation efficiency can be obtained from performing measurements in a Raman-inactive gas such as argon. Because argon is mono-nuclear, there are no resonant states that the probe can scatter from. This

means that all of the generated signal is non-resonant. It shows precisely which frequencies scattered from the argon and how often, translating to the available photon pairs in the pump/Stokes beam. This information can then be used to correct the data with.

3.2.5. Quantum efficiency

The camera sensor used to detect the signal does not detect all wavelengths with the same efficiency, meaning that a correction has to be applied manually after measuring. The corresponding quantum efficiency curve is given in figure 3.7. The CARS signal from hydrogen measured in this research is blueshifted at most 1000 wavenumbers for the S-branch transitions and redshifted at most 1500 wavenumbers for the O-branch transitions. With a central frequency of 400 nm, the region of interest corresponds to the 386 - 426 nm range, shown in figure 3.8. It is evident that the quantum efficiency varies greatly and thus the spectrum needs to be corrected. This correction is applied to the synthetic spectrum to avoid multiplying any inaccuracies in the measurement. It is worth noting that due to the quantum efficiency the recorded signal drops for the S-branch transitions but increases for the O-branch transitions, which is the opposite of the influence of the Placzek-Teller coefficients. However, the combined effect of the quantum efficiency and the Placzek-Teller coefficients still favours the S-branch transitions in terms of expected signal intensity.

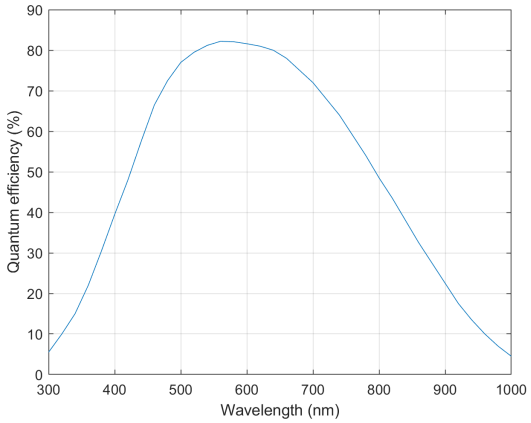

Figure 3.7: Quantum efficiency curve of the Andor Zyla 4.2 camera sensor.

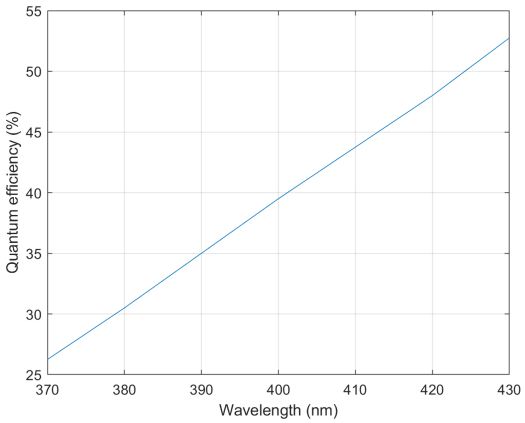

Figure 3.8: Region of interest of the camera's quantum efficiency.

3.2.6. Phase mismatch

The CARS signal beam is a result of the probe scattering from the rotational states coherently excited by the pump/Stokes beam. Early works on CARS utilized a co-linear arrangement for all beams where the phase matching condition is automatically satisfied (figure 3.9 and equation 3.17) [34].

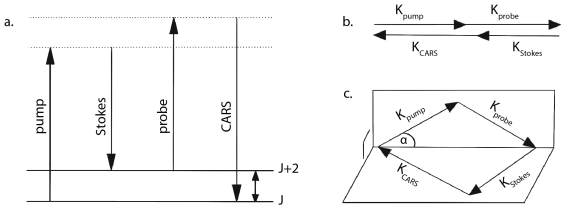

Figure 3.9: a. Energy level diagram, b. Co-linear CARS phase matching scheme, c. BOXCARS phase matching scheme.

$$\Delta k = (k_{pump} - k_{Stokes}) + k + probe - k_{CARS} \tag{3.17}$$

Here, k denotes the wave vector and Δk is the vector mismatch. $\Delta k = 0$ is the phase matching condition. Phase matching is important, because any phase mismatch decreases signal intensity according to equation

3.18.

$$Phase\ mismatch = \left(\frac{sin(\Delta kz/2)}{\Delta kz/2}\right)^2 \tag{3.18}$$

Purely co-linear setups are unable to resolve spatial data and filtering of the signal from the rest of the beams is required. Later works made progress on BOXCARS arrangements, intersecting the pump, Stokes and probe beams in a common intersection volume, giving a certain spatial resolution characterized by the size of the interaction volume. When two beams with different energies intersect at an angle, a vector mismatch is introduced. Luckily, this can be resolved by letting the third beam intersect this common volume at a certain angle following from the phase matching condition[43]. This has the benefit of giving each beam (including the signal beam) a distinct direction, relieving the need for filtering (figure 3.9).

The setup used in this research utilizes a two-beam CARS setup, where the pump and Stokes photon originate from the same beam. This simplifies beam focussing, but it also means a BOXCARS scheme is impossible to implement. A crossing angle θ between the pump/Stokes and probe beam inherently introduces a vector mismatch, shown in figure 3.10.

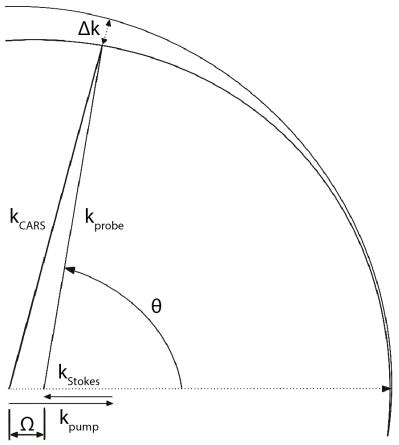

Figure 3.10: Phase mismatch depending on crossing in a co-linear pump/Stokes setup.

The degree of vector mismatch can be calculated by substituting equation 3.19 into equation 3.17.

$$k_{CARS} = \sqrt{\left[(k_{pump} - k_{Stokes}) + k_{probe} \cdot cos\theta\right]^2 + (k_{probe} \cdot sin\theta)^2} \tag{3.19}$$

The decrease in signal intensity scales with increasing phase mismatch, which in turn grows with Raman shift and crossing angle. The crossing angle is fixed, but the phase vectors are dependent on wavelength. The higher the wavenumber, the larger the influence of phase mismatch is. The CARS signal from hydrogen has large Raman shifts, making it important to account for this effect.

3.3. Raman transition line width

3.3.1. Pressure broadening

The exponential decay of the molecular response is caused mainly by the exchange of energy through collisions of the molecules. These collisions cause some molecules to have slightly higher or lower rotational energy, changing their measured Raman shifts. This behaviour is taken into account by the Raman transition line width $\Gamma^{(k)}_{J\rightarrow J+2}$. Determination of this parameter can be done experimentally through picosecond CARS by measuring the decay at different pump/probe delays. Such an approach has also been used by Kliewer *etal* to determine the Raman transition line widths for nitrogen at different temperatures. In their paper, they present tables with the values for $\Gamma^{(k)}_{J\rightarrow J+2}$ at different temperatures and for different rotational states. These are the values that are also used in this thesis. For hydrogen, the exponential decay is many order of magnitude slower and is barely perceived at all on a picosecond timescale.

3.3.2. (Thermal) Doppler broadening

Thermal Doppler broadening is the cumulative effect of emission by particles with varying Doppler shifts. These Doppler shifts are caused by the particles random thermal motion, imparting a velocity distribution [55],[56]. When the emitting particle moves towards a stationary observer, its perceived frequency increases. When the emitting particle moves away from a stationary observer, its perceived frequency decreases. The thermally induced velocity distribution in turn causes a distribution in the perceived frequency, which is thermal Doppler broadening. The larger the velocity distribution, the larger the effect of thermal Doppler broadening. This effect is especially relevant for lighter molecules such as hydrogen, because they move faster.

3.3.3. Probe pulse duration

For molecules with a rapidly decaying molecular response, the spectral line width is heavily influences by the rate of decay, because it limits the amount of periods that can be sampled, thus introducing an uncertainty. The faster the molecular response decays, the larger the uncertainty. In the case of hydrogen, however, the molecular response has an incredibly long life-time in the order of nanoseconds. This means that given a long enough sampling time, the spectral line width can be very small. In such a case, the spectral line width is determined by the sampling time, which is the probe duration. Figure 3.11 shows the overlap of the probe pulse with a molecular response.

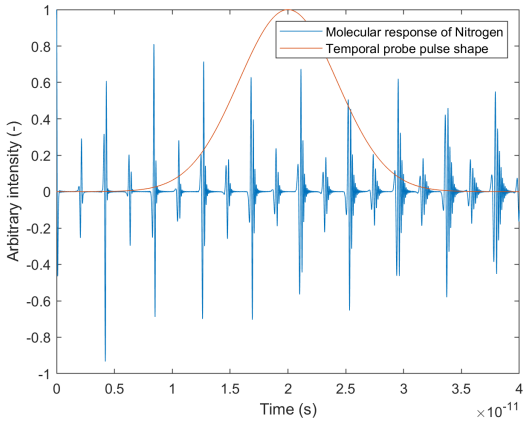

Figure 3.11: The temporal overlap of the probe pulse with the molecular response.

In order to model the probe, its duration has to be measured first. Unfortunately, the pulse duration is much too short to measure directly. Instead, measurements are done in argon with a varying pump/probe delay. The temporal overlap of the probe pulse with the non-resonant argon signal determines the signal intensity. The change in signal intensity as a result of the varying delay is a direct indicator of the temporal shape of the probe pulse.

3.3.4. Instrument Response Function

The Instrument Reponse function is a correcting function that links the measured quantities of detected events to the physical quantities of the incident photons. Probabilities are assigned that a detected event is indeed a photon. Here, the probabilities are dependent on both the hardware used to detect the events as well as the software used to process the event parameters. The Instrument Response Function can be thought of as an area times a probability that an incident photon is indeed detected as an event with measurable physical quantities. In the code, this can be implemented as a convolution with a Voigt profile, which is a convolution of a Gaussian and Lorentzian profile, each shown in figure 3.12. The equations for the Gaussian and Lorentzian line shapes are given in equations 3.20 and 3.21.

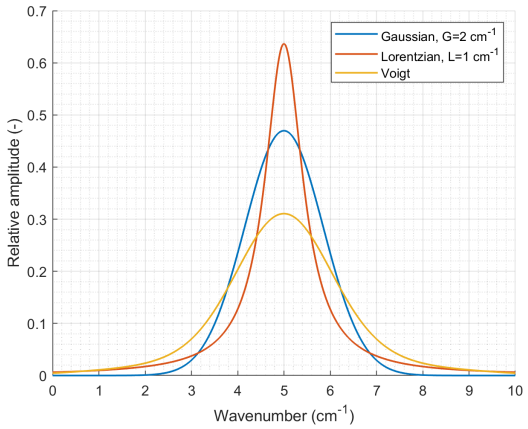

Figure 3.12: The shapes of the Voigt, Gaussian and Lorentzian profiles

$$Gaussian = \frac{2\sqrt{ln(2)}}{G \cdot \sqrt{\pi}} \cdot e^{\frac{-\left[(\omega-\omega_0)\cdot 2\sqrt{ln(2)}\right]^2}{G^2}} \tag{3.20}$$

$$Lorentzian = \frac{L}{2\pi\left[(\omega-\omega_0)^2 + \frac{L}{2}\right]} \tag{3.21}$$

Convolving the synthetic spectra with these line shapes induces numerical line broadening to obtain good accordance with the data. The influences of each contribution, G and L, can be tuned to achieve a proper fit. A well resolved known spectrum (such as room temperature air or nitrogen) is taken for calibration purposes to reconstruct values for both the Gaussian and Lorentzian influences of the Voigt profile, which are then also used in the fitting model.

3.4. Synthetic spectra

Using the code explained above, synthetic spectra can be generated for the molecular response of a given molecule for a given temperature. Due to differences in molecular constants, every molecule has a different molecular response and hence produces a different spectrum. Figure 3.13 shows the spectra for both nitrogen and hydrogen for a temperature of 700 K and clearly shows the differences between the two spectra.

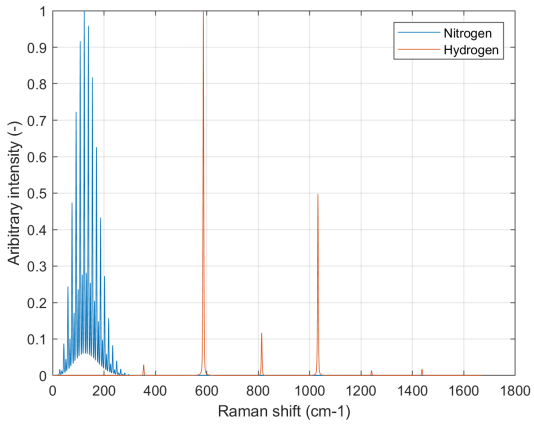

Figure 3.13: CARS spectra corresponding to the molecular response of nitrogen and hydrogen at 700 K.

Nitrogen populates many more rotational states than hydrogen, but the energy spacing between them is much smaller. In the spectrum this is shown by the many closely spaced peaks in the nitrogen spectrum, as opposed to the few widely spaced peaks in the hydrogen spectrum. Another thing to note is the degree of

isolation of both the nitrogen and hydrogen peaks. When spectral line broadening effects occur for nitrogen, the widening of the peaks quickly causes the signals of adjacent peaks to overlap, making the individual peaks less pronounced. Hydrogen on the other hand, has very isolated peaks in the spectrum that practically never overlap.

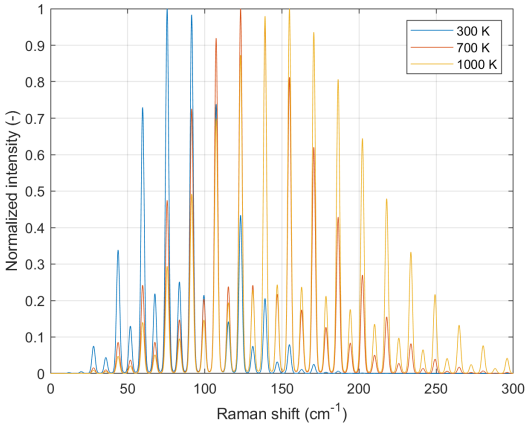

Figure 3.14: The nitrogen S-branch for different temperatures.

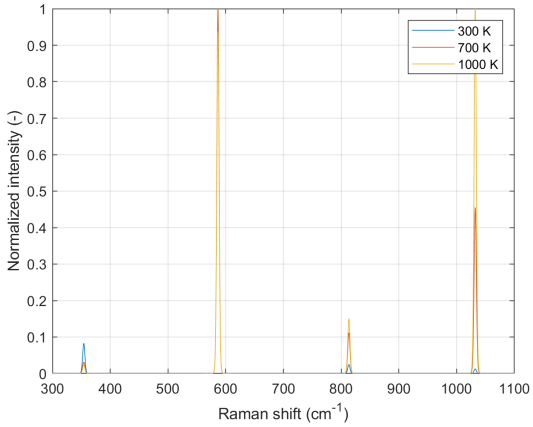

Figure 3.15: The hydrogen S-branch for different temperatures.

Figures 3.14 and 3.15 show the influence of temperature on the different spectra. As the temperature increases, the spectra shift to higher Raman shifts because of the Boltzmann population distribution. For nitrogen, a clear spectral envelope can be discerned that gradually shifts with increasing temperature. The many different spectral peaks can all be used for temperature evaluation. For hydrogen, this envelope is not as pronouced because of the few peaks present in the spectrum. Especially at lower temperatures, most of the signal is coming from S(0) and S(1). Moreover, spin degeneracy causes odd rotational states of hydrogen to be populated three times as much as the even rotational states, making for a large difference in relative signal intensity. These effects make low temperature fitting of hydrogen very dependent on the accuracy with which S(0) can be determined, because small deviations in S(0) relative to S(1) translate to large differences in evaluated temperature. At higher temperatures the Boltzmann population distribution shifts. This quickly causes the signal in S(0) to diminish, making thermometry purely based on S(0) and S(1) impossible for higher temperatures. While the signal intensity in S(0) dies down, the population shifts towards S(2) and S(3). In the 700 - 1000 K range, the accuracy of hydrogen thermometry depends mostly on the accuracy with which S(3) can be determined, as it is the second strongest peak after S(1). For higher temperatures, more rotational states become populated on which spectral fitting can be performed.

In order to perform spectral fitting, the experimental spectrum is compared with a number of different synthetic spectra. To this end, libraries are compiled that contain a large number of different synthetic spectra depending on the fitting parameter. These fitting parameters are usually temperatures and species concentrations, but libraries can also be compiled for varying probe delays or different Instrument Response Functions. Once the libraries are compiled, they can be compared quickly and efficiently with an experimental spectrum to find the best fit. This process will be explained in more detail in the next chapter.

4

Experiments

This chapter describes the experimental portion of the thesis, and all things related. First the experimental setup will be discussed, after which the experiments will be outlined and the data processing protocol will be elaborated upon. These results will then be presented in the next chapter.

4.1. Experimental Setup

The research was done using a two beam hybrid fs/ps CARS setup, capable of performing 1-dimensional spatiotemporal CARS measurements at a repetition rate of 1 kHz. Hybrid fs/ps CARS imaging has already been applied for multi-species gas phase thermometry by Bohlin et al [28], but these experiments were performed at a very low repetiton rate. Castellanos et al [33] already performed hybrid fs/ps spatiotemporal CARS measurements at 1 kHz repetition rates, but performed thermometry exclusively on nitrogen and oxygen. Additionally, Courtney et al [38] have used two beam hybrid fs/ps CARS to perform hydrogen thermometry at 1 kHz, but used point measurements to do so. This research marks the first time a two beam hybrid fs/ps CARS setup is used to perform spatiotemporal hydrogen thermometry at such a high repetition rate.

The setup itself is shown in figure 4.1. All lasers used in the setup originate from a single laser source, to minimize jitter between the beams. After amplification the beam is split into two: one will become the pump/stokes beam, the other the probe beam.

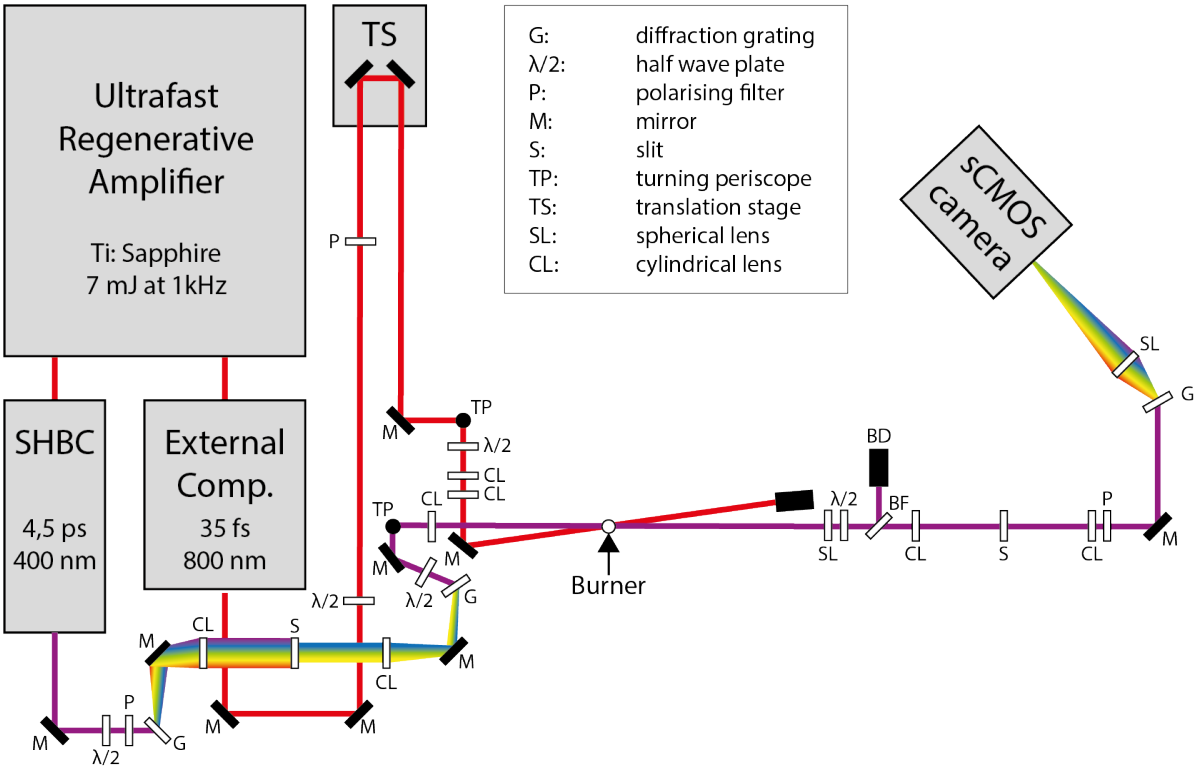

Figure 4.1: Diagram of the experimental setup.

After the ultrafast regenerative amplifier, the beams consist of chirped 800 nm, 100 fs pulses at a repetition rate of 1 kHz. When the beams are split, 35% of the power is used for the pump/Stokes beam and 65% of the power is used for the probe beam. The pump/Stokes beam passes through an external compressor, which compresses the pulses to its near-transform limit at 35 fs. The beam then passes through a half-wave plate and polarizing filter combination, which is used to tune the power of the beam. The beam then travels to the translation stage and back. The translation stage is a very sensitive remote controlled linear stage which can shorten or lengthen the beam path to effectively change the arrival time of the pulses on the order of picoseconds. The beam then passes through a second half-wave plate, which is used to set the final polarization of the beam. In figure 4.1, the beam passes through two cylindrical lenses, which is the arrangement used to perform CARS imaging. The two cylindrical lenses have equal focal distances, but are placed so that their focal axes are perpendicular to each other. The first lens focusses the beam into a line in the probe volume. The second lens also converges the beam, but because its focal point is positioned just behind the burner, the beam never gets focussed into a point. Instead the beam gets focussed into a very short line (order of a millimeter in length), in order to increase the intensity. It is now possible to perform CARS measurements over a line instead of in a single point, yielding additional spatial information in a single dimension.

In the case of point measurements, these two lenses are replaced with a single spherical lens that focusses the pump/Stokes beam in the probe volume, right above the burner. The spherical lens causes the beam to focus to a point, ultimately gathering information only from that point. If the beam intensity becomes high enough, filamentation occurs which produces an ultra-broadband pulse.

Filamentation is the continuous self-focussing and defocussing of an intense laser beam. The index of refraction for air is dependent on the intensity of a present electromagnetic field (equation 4.1). The intensity is usually highest in the center of the beam, gradually decreasing towards the waist. This effectively turns the air it travels through into a lens, focussing the beam if n_2 is positive. Normally, this effect is not observed because the effect of diffraction is greater. However, for a certain critical power (equation 4.2) the effect of self-focussing outweighs the effect of diffraction and the beam will collapse onto itself. The varying refractive index also induces a varying phase shift in the pulse, which broadens the frequency spectrum[39].

$$n = n_0 + n_2 \cdot I(r,t) \tag{4.1}$$

$$P_{cr} = 3.72\lambda_0^2/(8\pi n_0 n_2) \tag{4.2}$$

During the self-focussing process, the intensity of the beam increases. At a certain point, the intensity is sufficiently high so that photo-ionization can occur. Photo-ionization requires the simultaneous absorption of multiple photons and is thus strongly dependent on the intensity of the beam. The onset of photo-ionization is often very abrupt and creates a local underdense plasma, which locally reduces the index of refraction, in turn causing defocussing of the beam.

After defocussing, the beam can still have sufficient power to undergo self-focussing again, repeating the cycle as shown in figure 4.2. This continues until multiphoton absorption reduces the beam power below P_{cr}. The filament is said to be the region of self-focussing and defocussing cycles.

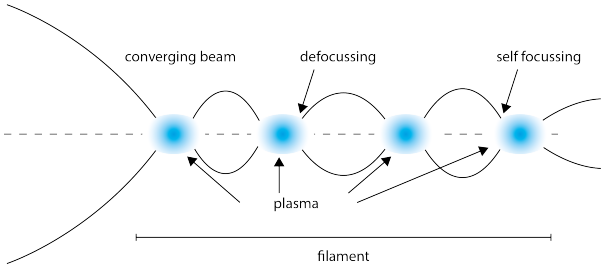

Figure 4.2: The continuous self-focussing and defocussing of an intense light beam.

After the focussing lenses (whichever setup is used), a mirror is used to guide the beam towards the probe volume. The position of this mirror also dictates the crossing angle between the beams, and therefore the interaction length of the beams and the degree of phase mismatch. After the interaction volume there is no more use for the pump/Stokes beam and it is discarded into a beam dump.

The second portion of the intial 800 nm, 100 fs beam that will become the probe beam is guided towards the Second Harmonic Bandwidth Compressor (SHBC). This component effectively transforms the broadband 800 nm beam into a narrowband 400 nm beam through Sum Frequency Generation (SFG). Inside the SHBC, the beam is split 50/50. Each of these beams are then diffracted by means of a diffraction grating and imparted with equal but opposite (approximately) linear chirp. These chirped pulses are then recombined in a Beta Barium Borate (BBO) crystal. The higher frequencies in one pulse are combined with the lower frequencies in the other pulse and vice versa, resulting in a narrowband pulse centered around double the initial frequency. This narrow bandwidth is a result of the slightly non-linear chirp induced by the SHBC. This process is explained is much greater detail in the papers by Courtney et al [31] and Thorn et al [32]. The chirped 800 nm, 100 fs beam that entered the SHBC exits as a 400 nm, 4.5 ps beam at the near-transform limit. The probe then travels through a half-wave plate and polarizing filter combination that acts as an attentuator to tune the power of the beam. The beam then passes through a combination of diffraction grating, cylindrical lens, slit, cylindrical lens and grating also known as a 4f filter[41]. The beam is diffracted and subsequently focussed in the fourier plane using a cylindrical lens. The slit is located in the fourier plane and closing the slit allows shaping of the pulse by cutting off the outer frequencies. This allows further narrowing of the bandwidth, but also reduces the pulse energy as a portion of the light is simply blocked. The main use of this configuration is cutting off any unwanted effects that might be produced by the non-linear chirp in the SHBC, leaving a near Gaussian probe pulse. The subsequent cylindrical lens and grating do the same, but in reverse, combining the light back into a narrowband pulse. The probe beam then travels through a second half-wave plate, which sets the polarization of the beam. In the case of CARS imaging, a cylindrical lens is used to also focus the probe into a line, otherwise a spherical lens is used to focus to a point.

The pump/Stokes and probe beams intersect in a common volume known as the interaction volume or probe volume. The physical size of this volume dictates the spatial resolution of the measurements, as it is impossible to tell where in the interaction volume a certain photon scattered from. Typically the height and width of

the interaction volume in this setup is on the order of 50 microns, while the interaction length is on the order of a millimeter due to the shallow crossing angle of the beams. In CARS imaging, the height of the interaction volume extends to 1-3 millimeters, which can be thought of as many small interaction volumes stacked on top of one another.

After leaving the interaction volume, the probe and the CARS signal travel co-linearly, inherent to using a two beam CARS setup. A lens collimates the beam and a half-wave plate is used to set the polarization of both beams (not independently). In order to evaluate the signal, the probe needs to be separated from the signal as much as possible. The intensity of the probe is around 5 to 6 orders of magnitude higher than the intensity of the CARS signal and aiming it directly into the camera would burn out the sensor almost instantly. To achieve this, a band-pass filter is placed in the beam path, which either reflects or transmits light based on its frequency[45]. Light in the pass-band is transmitted entirely while light in the stop-band is reflected by 7 orders of magnitude. In between the pass- and stop-band however, is a transition region where the light is gradually transmitted more and more. This region is not well defined and careful consideration of the wavelengths affected by this transition region must be taken into account. Next, the beam travels is focussed in the opening of a slit, which aims to suppress any stray light. A subsequent lens recollimates the beam. The beam then passes through a birefringent crystal, which splits the beam based on the polarization of the colinear beams.

The polarization state of the CARS signal is a result of the combined effect of the polarization states of the probe beam and pump/Stokes beam[47]. By tuning the polarization, the resonant CARS signal, non-resonant CARS signal, pump/Stokes and probe beams can all have different polarization angles and individual angles can be optimized for filtering depending on the needs of the setup. In three beam CARS, this property is often used to induce a maximum polarization difference between the resonant and non-resonant signal, which allows isolation of the resonant signal[48]. In hybrid fs/ps setups, the contribution of the non-resonant CARS signal is negligible due to the temporal isolation of the probe pulse. Instead, the polarization can be tuned to induce a maximum difference in polarization angle between the probe beam and the resonant CARS signal. This enables splitting of the resonant CARS signal from the probe beam.

The signal beam then travels through a transmission grating, diffracting the light. A subsequent lens focusses the light in the fourier plane on the camera lens, allowing for measurement of the intensity of the spectral content of the signal. The sensor itself is unable to differentiate between different wavelengths, but knowledge of certain prominent peaks in the spectrum or calibration beforehand give the required information to convert the pixel coordinates to wavenumbers. The spectral resolution is determined by the amount of pixels over which the signal is spread. A higher spectral range results in a lower spectral resolution and vice versa.

4.2. Procedure

While the thesis is on the spectroscopy of hydrogen, no hydrogen was available in the lab; only methane could be used. Luckily, hydrogen can be produced by (partially) oxidizing methane according to the reaction pathways given in figure 4.3. The pathways that are favoured, heavily depend on the temperature, pressure, concentration and possibly the use of catalyzers during the reaction [27].

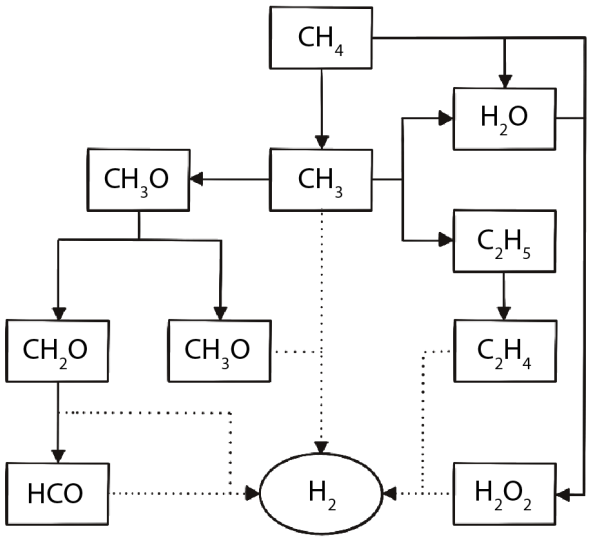

Figure 4.3: Methane to hydrogen chemical reaction pathways [26].

When methane is combusted with air under normal conditions, it reacts with the oxygen in the air to produce carbon dioxide and water vapour. The ideal reaction formula is described in equation 4.3. However, when the combustion happens in an oxygen-poor environment, for example under rich premixed conditions, the ideal reaction formula competes with the partial oxidation of methane given in equation 4.4 [25]. Both reactions are exothermic at atmospheric conditions and require no additional energy input, as compared to steam reforming or CO_2 reforming of methane which are not feasible in our lab. The degree to which the two equations compete with one another depends mostly on the temperature, pressure and equivalence ratio, higher values for which all favour the partial oxidation of methane [29] [30].

$$CH_4 + 2\,O_2 = CO_2 + 2\,H_2O \tag{4.3}$$

$$CH_4 + \frac{1}{2}O_2 = CO + H_2 \tag{4.4}$$

The burner setup is shown in more detail in figure 4.4. The burner used in the experiments is a one meter long metal tube with an inner diameter of 10 mm and a chamfered edge. The burner is mounted on a linear stage which is in turn mounted to the table. This allows for very precise positioning of the burner with respect to the probe volume. The fuel and air are premixed before being sent to the burner. Both the fuel and air have their own storage tank and flow controller, so that the flow rates and equivalence ratio's can be independently regulated. The flows are regulated by use of rotameters, after which the flows are mixed in the flame arrester. The bulk flow rate of the gas mixture during the experiments was $1 m/s$, at an equivalence ratio of 1.58. This gives a Reynolds number for the flow of around 650. The large aspect ratio of the straight pipe allows the flow to be fully developed when it reaches the end of the burner tube. Even though a very high equivalence ratio is desired, flame stability imparts an upper limit of how rich the flame can be. The equivalence ratio of 1.58 was found experimentally to be the best trade-off between flame stability and equivalence ratio. The resulting flame was laminar but flickering slightly, as can be seen in figure 4.5.

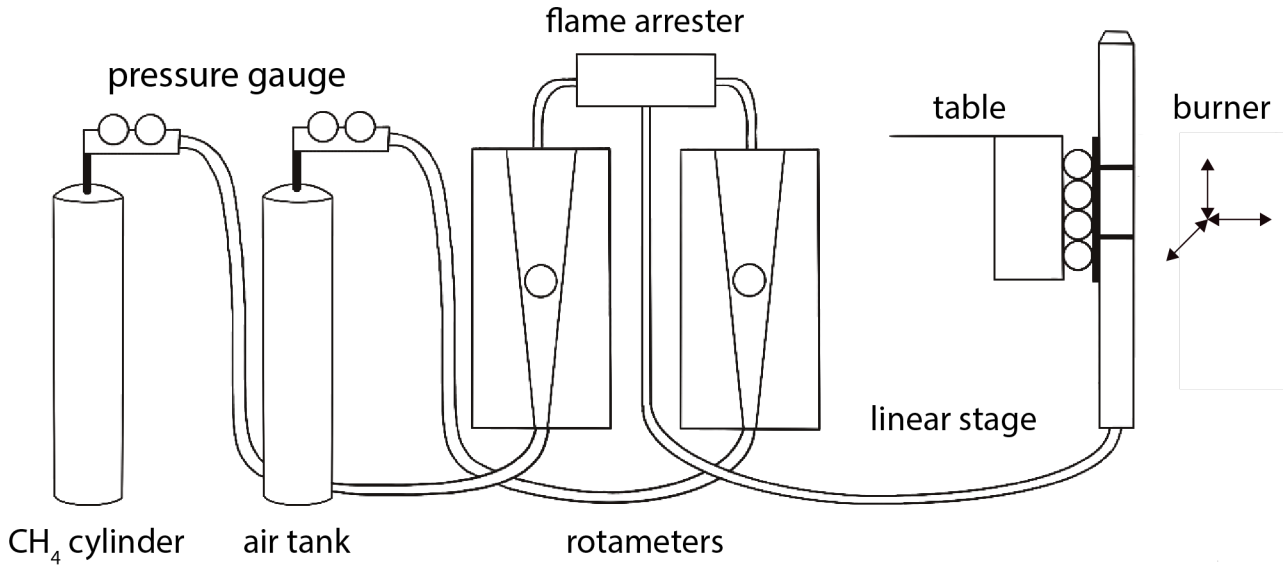

Figure 4.4: Schematic drawing of the burner and flow controllers.

Figure 4.5: The Bunsen burner flame used in the experiments.

Figure 4.6: Filament visible in the flame (Image courtesy of Nathan Griffioen).

Because of the high equivalence ratio, there exist two combustion zones in the flame. The inner combustion cone where the methane primarily reacts with the premixed air and the outer combustion zone, where the excess fuel burns with oxygen from the surrounding air to produce a diffusion flame. The two regions are clearly visible in figure 4.5. The measurements are done in the inner flame cone. The inner flame cone preheats the cold mixture prior to combustion, giving rise to a temperature gradient from the rim of the burner to the tip of the flame. This allows probing of different conditions within the same flame.

The experiments can roughly be subdivided into three categories, according to the type of excitation that was used. The first set of experiments used line measurements, where the broadband pump/Stokes and probe beams are focussed in a line to perform CARS imaging. This gives 1 dimension of spatial data as well as temporal data, but sacrifices signal intensity. The second set of experiments was done using an ultrabroadband pump/Stokes beam where the beams were focussed in a point to form a filament. The ultrabroadband beams are able to excite higher Raman transitions than regular broadband excitation, but the method is less robust. Figure 4.6 shows the filament focussed in the reactants side of the flame. The last set of experiments was done using a broadband pump/Stokes beam focussed in a point. This method sacrifices spatial data for signal intensity when compared to the first method and sacrifices excitation range for excita-

tion stability when compared to the second method.

4.2.1. Data processing

After the experiments have been performed and data has been recorded, the camera images can be processed. Figure 4.7 shows an example of what a recorded signal looks like in the camera. The signal corresponds to a room temperature nitrogen spectrum, which is shown here because of its clarity. Figure 4.8 shows the same data exported to Matlab.

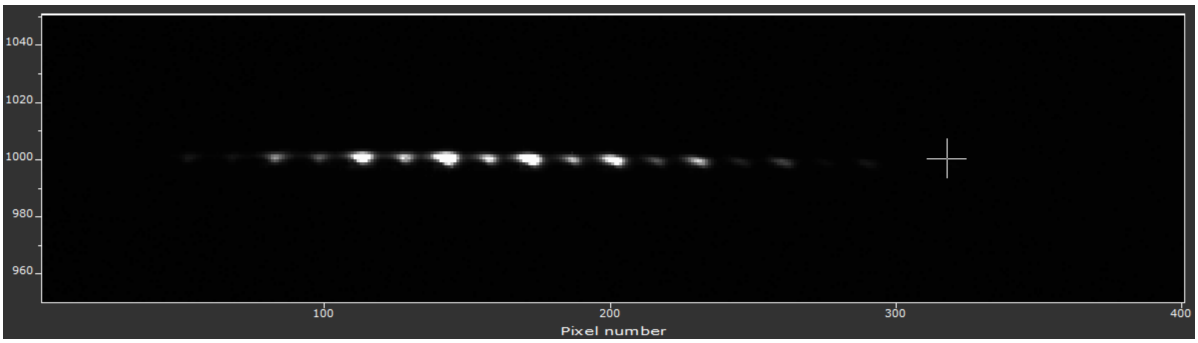

Figure 4.7: A recorded room temperature nitrogen spectrum.

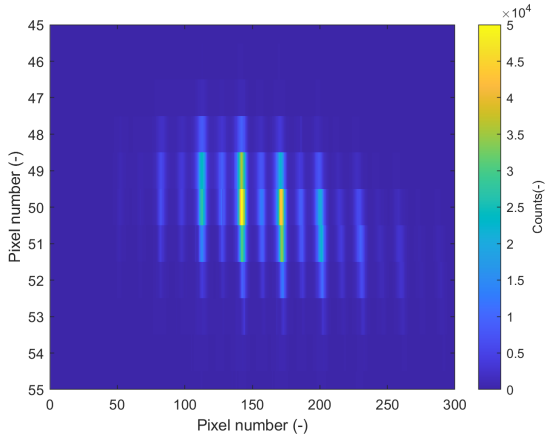

Figure 4.8: The exported nitrogen spectrum shown in MatLab.

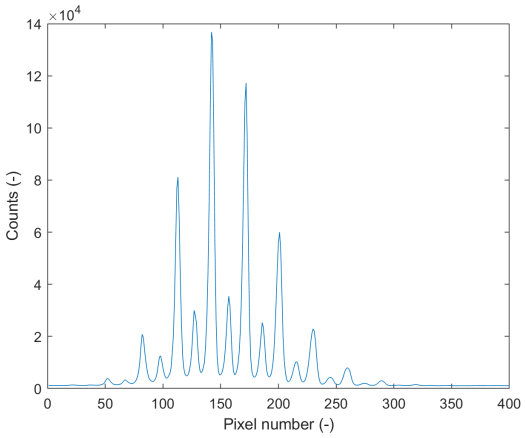

Figure 4.9: Vertically binned data extracted from the camera

Unfortunately, what is recorded by the camera cannot be directly compared to the synthetic spectrum. Even though this data is the result of a point measurement, the signal is spread over multiple pixels. The pixels in the y-direction hold spectral information, but the pixels in the x-direction hold no additional information for point measurements. To capture the signal in its entirety, the signal is binned vertically. This leaves the data shown is figure 4.9. This data still cannot be compared to the synthetic spectra, because what is output by the camera is roughly comprised of a background signal, some random read noise and the actual signal itself. To compensate for the background signal, a separate measurement can be done to record only background signal. A number of different frames can be recorded after which they are averaged and subtracted from the original signal. This is shown in figures 4.10 and 4.11.

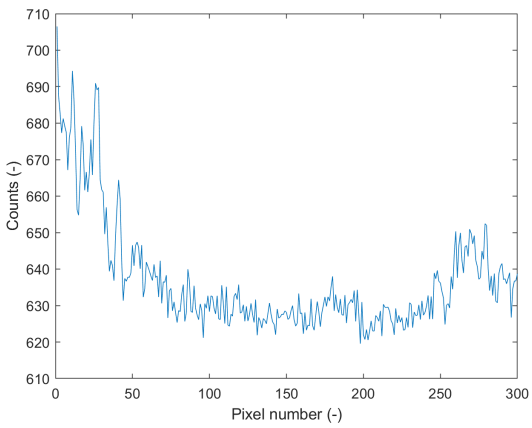

Figure 4.10: The average background signal.

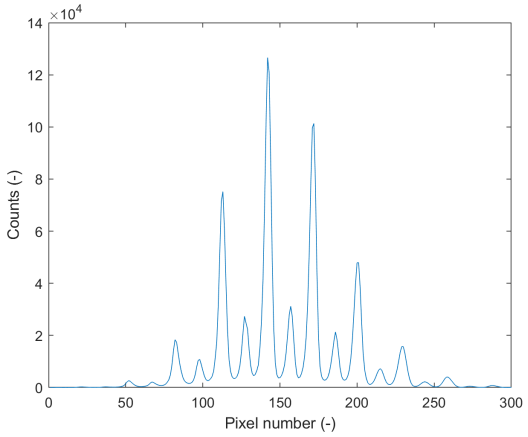

Figure 4.11: The experimental data with background subtraction.

The random read noise can be mitigated somewhat by binning over several pixels vertically, horizontally (or both) or averaging over multiple single shot measurements, but doing so will negatively affect the spatial, spectral or temporal resolution respectively. It must be noted that the decrease in spatial resolution is only applicable to CARS imaging (line measurements). Once the background has been subtracted, the signal needs to be normalized with the excitation efficiency of the pump/Stokes beam. The excitation bandwidth and profile of the pump/Stokes beam dictate which resonant states are excited and how strong this excitation is. The model that is used to produce the synthetic spectra does not take this influence into account and instead assumes infinite and uniform excitation. To match the experimental data to the synthetic spectrum, this effect needs to be taken into account.

Measuring the excitation efficiency is done by performing a measurement in Argon. Argon has no Raman active modes, and therefore only produces a non-resonant signal. Referring to the energy level diagram in figure 5.46, it is clear that the non-resonant signal can only be produced where the pump/Stokes beam can excite a non-resonant transition. Therefore, the non-resonant signal in Argon is a direct measurement of the excitation efficiency. The recorded non-resonant Argon signal also experiences a background signal, which can be compensated for in the same way as before. Assuming the excitation efficiency is steady in time, the signal is averaged over multiple shots to minimize the random read noise. The excitation efficient measured for this data set is shown in figure 4.12. Finally, the experimental data can be normalized with the non-resonant Argon signal. The difference between the raw camera data and the final normalized spectrum is shown in figure 4.13.

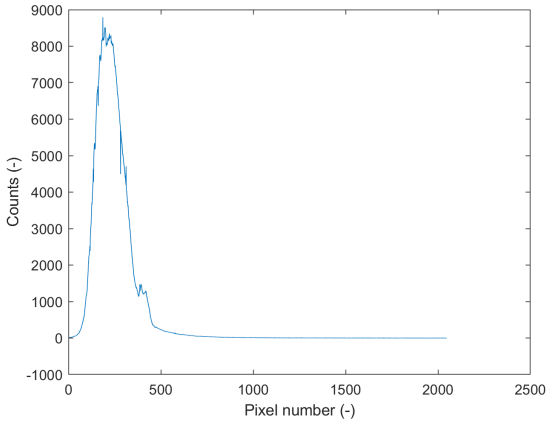

Figure 4.12: The average non-resonant signal in Argon.

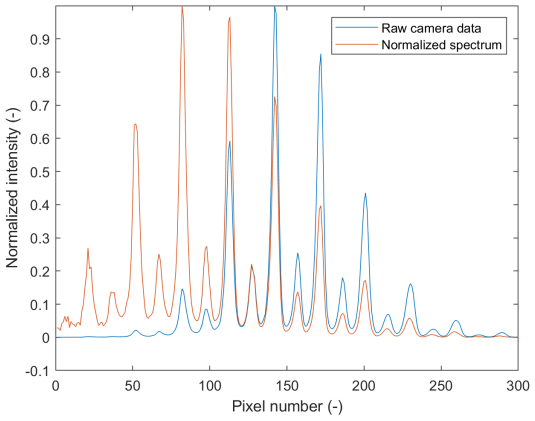

Figure 4.13: The raw data vs the normalized spectrum.

Once the experimental data has been normalized, the pixel coordinates need to be converted to wavenumbers. This can be achieved by identifying certain known peaks in the signal and calculating the spectral reso-

lution from there. For room temperature Nitrogen, S(6), S(8), S(10) and S(12) are easily identified as they are the highest four peaks. The Raman shifts corresponding to these positions are well documented, allowing accurate conversion of pixels to wavenumbers. The Raman shifts corresponding to the experimental spectrum are shown in figure 4.14.

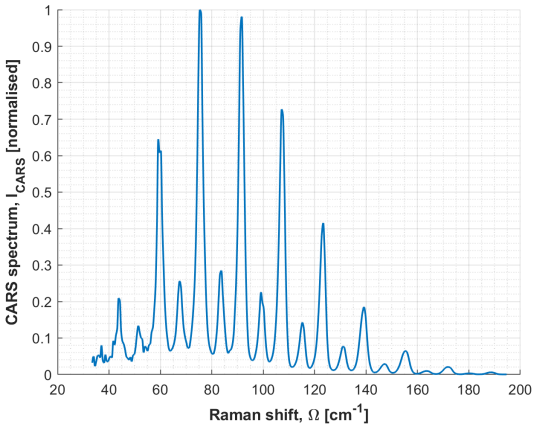

Figure 4.14: The normalized experimental spectrum with pixel coordinates converted to wavenumbers.

Once the pixel coordinates have been converted, the experimental data is ready to be evaluated. The experimental data is compared against every spectrum in the synthetic library and the sum squared residual (SSQ) is computed each time. A minimum value for the SSQ indicates the best fit and therefore the corresponding combination of fitting parameters also applies to the experimental spectrum. In the figures below two close fits are shown for the experimental spectrum, one where the temperature is slightly underestimated, and one where the temperature is slightly overestimated. The black line below the fits shows the residuals, or the discrepancy in the fit.

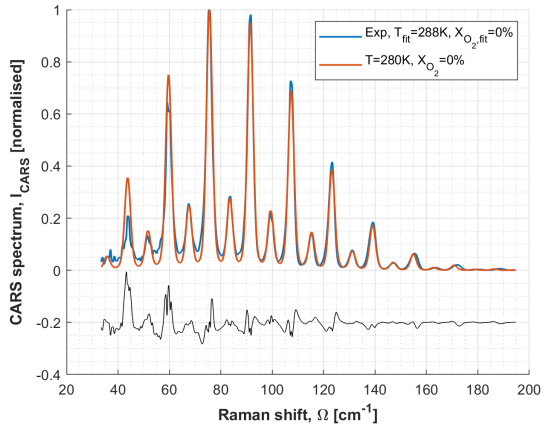

Figure 4.15: A slightly underestimated temperature fit.

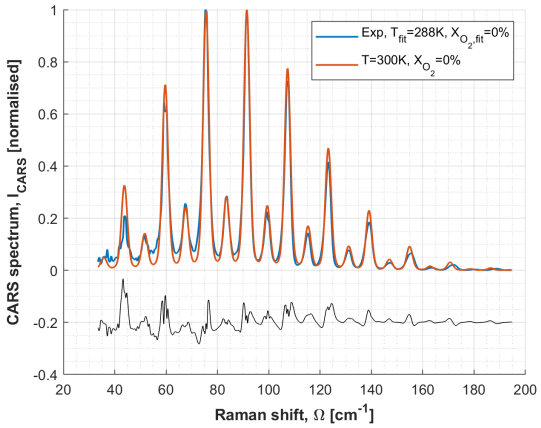

Figure 4.16: A slightly overestimated temperature fit.

Figure 4.15 shows the data with a slightly lower temperature fit, which can be identified from the consistent undershoot at higher Raman shifts. Figure 4.16 on the other hand shows a slightly higher temperature. This can be identified from the consistent overshoot at higher Raman shifts. Another thing to note from both of these fits is the consistent overshoot for both fits at lower Raman shifts. This is because the experimental spectrum is affected by the band-pass filter in this region, leading to a lower signal intensity. The presence of the band-pass filter is very noticeable at 40 cm^{-1}, but gradually weakening until it is barely affecting the spectrum anymore at around 80 cm^{-1}. When performing spectral fitting, it is paramount to be aware of such effects so they can either be excluded from the fit or be accounted for. Attempting to fit the affected part of the spectrum would yield very misleading conclusions.

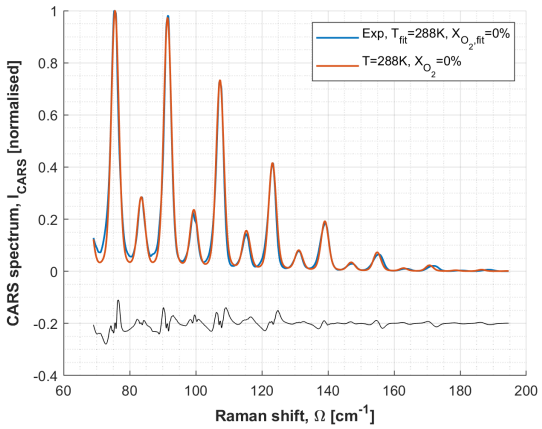

Figure 4.17: The best fit for the room temperature Nitrogen spectrum.

Figure 4.17 finally shows the best fit, and thus the evaluated temperature. The data processing protocol is mostly the same for all measurements, with the exception of CARS imaging. Where the nitrogen room temperature spectrum was vertically binned for a stronger signal, spectra obtained through CARS imaging will be evaluated row by row, where each row corresponds to a location along the measurement line. These results, along with the rest of the data acquired will be presented in the next chapter.

5

Results and discussion

In this chapter, the results of all experiments are presented and discussed. First of all, the validity of the theoretical model and the synthetic spectra they produce has to be verified. There is no use in comparing Hydrogen thermometry to Nitrogen thermometry when neither is sure to give the right temperature. To this end, the Nitrogen and Oxygen models are tested by predicting two known spectra at a known temperature: a room temperature spectrum of pure Nitrogen and a room temperature spectrum of air. Once these cases yield accurate results, the actual data containing both the Hydrogen and Nitrogen spectra can be assessed.

5.1. Calibration spectra

The previous chapter showcased a room temperature pure Nitrogen spectrum to demonstrate the data processing and fitting procedure. At the end of the chapter, the temperature was evaluated at 288 K. The second validation is the measurement in room temperature air. As shown in figure 5.1, a close fit was achieved again. The temperature was evaluated at 285 K, similar to the temperature that was found as in nitrogen, but this time the mixture also contained 20% oxygen by volume.

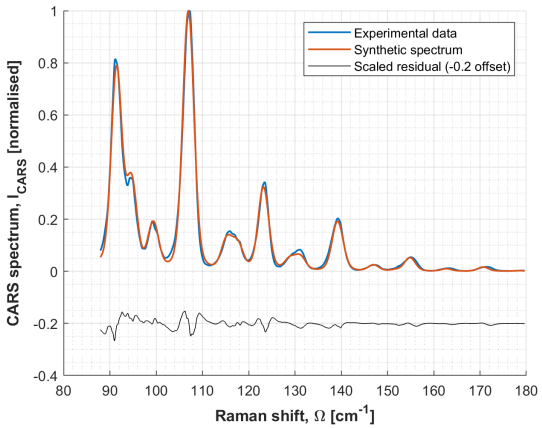

Figure 5.1: Best fit for room temperature air (285 K and 20% Oxygen).

The temperatures that are evaluated are slightly below room temperature, but the gases are stored in pressurized tanks at room temperature. As the gases exit their tanks they expand and are cooled as per the ideal gas law. As the gases flow through the tubing they heat back up a little bit, but can never exceed room temperature. Therefore, the slightly lower temperature is assumed to be accurate. With the Nitrogen and Oxygen models accurate predicting the calibration cases, it is time to compare the Nitrogen thermomemtry to the Hydrogen thermometry. As explained before, four different types of experiments were done: broadband line measurements, ultra-broadband point measurements, broadband point measurements and finally ultra-broadband point measurements on the CSRS side. The next sections present and discuss the results from each experiment separately.

5.2. Broadband line measurements (CARS imaging)

The first set of experiments that were done were line measurements, because the experimental setup was still in that configuration. The underlying physics are exactly the same for line measurements as point measurements, only the interaction volume changes. For line measurements, all lasers are focussed to a line, making the interaction volume elongated in the direction of this line. An example of the image produced by these measurements is shown in figure 5.2. Compared to figure 4.7, the signal is stretched in the vertical direction. Each row of pixels in figure 5.2 holds spectral information about a specific point on the measurement line, allowing the monitoring of the change of temperature and concentration with distance. Typically, the length of the measurement line and thus the spatial range is on the order of a millimeter. Depending on the amount of pixels the signal spans over and the binning that is applied, the temperature gradient over the measurement line can be determined in 10-50 μm increments. In this particular experiment, the resolution was 30 μm.

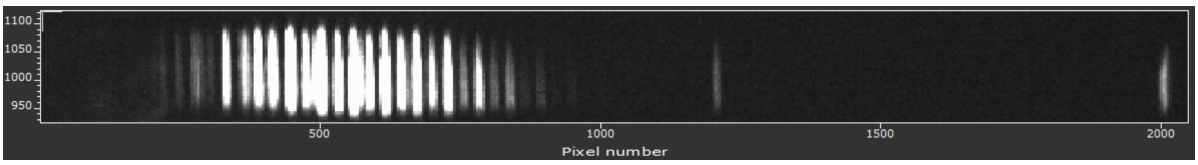

Figure 5.2: An example of Nitrogen and Hydrogen spectra recorded with CARS imaging.

Inherent to CARS imaging, the beam intensities are much lower than with point measurements, because the beams are focussed in a much larger interaction volume. Hence, the signal intensity in CARS imaging is also much lower. To obtain an adequate signal for hydrogen in single-shot mode, 4x4 binning was required. The still relatively weak S(0) and S(1) can be seen at approximately 1200 and 2000 pixels numbers, respectively. The nitrogen signal was close to saturating the camera at 60.000 counts, whereas S(0) and S(1) came in at approximately 300-500 and 600-1100 counts. With the background signal at 170 counts and the random noise fluctuating between 0 and 60 counts, the actual intensity of S(0) is very uncertain. Combined with the fact that hydrogen thermometry based solely on S(0) and S(1) is extremely sensitive on the value of S(0), the random noise alone made it so no meaningful data could be extracted from the hydrogen spectra. The nitrogen spectra on the other hand were very clear and allowed for spectral fitting. Figure 5.3 shows the evaluated Nitrogen temperature over the measurement line (y-axis) during a measuring time of 1 second at a 1kHz repetition rate (x-axis). Here, the pixel rows correspond to the vertical pixel numbers 1051-944 in figure 5.2.

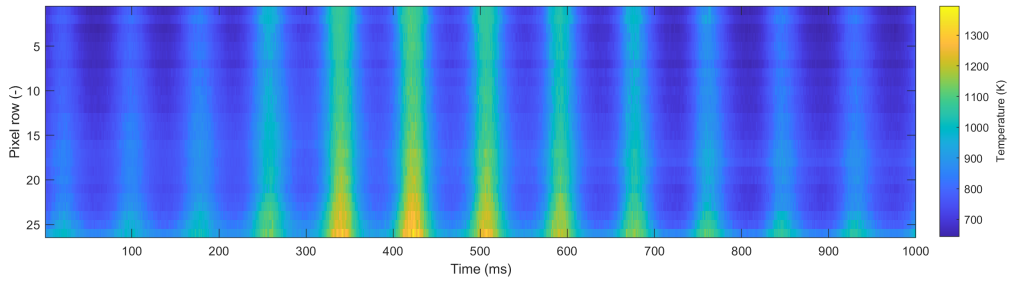

Figure 5.3: Nitrogen temperatures from the CARS imaging data.

A clear temporal pattern can be identified and Fourier analysis reveals a ~12 Hz and a ~1 Hz signal present in the data. The 12 Hz signal is a similar result as the one obtained by Castellanos et al [33], where they speculated the cause to be an instability in the local equivalence ratio. The 1 Hz signal could possibly be explained by flow instabilities caused by the rotameters, which can be seen oscillating at this frequency. However, more research is needed to confirm this theory.

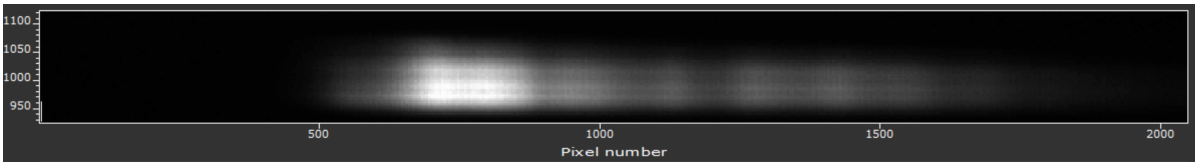

Figure 5.4: The non-resonant signal in Argon for the CARS imaging experiments.

In an attempt to explain the low hydrogen signal intensity, the experimental data and synthetic hydrogen spectra were more closely inspected. First of all, the recorded non-resonant signal in Argon (figure 5.4), indicative of the excitation efficiency, showed almost no excitation beyond Raman shifts of 550 cm^{-1}, causing the weak signal in S(1). Closer inspection of the synthetic hydrogen spectrum revealed that the population in the first rotational level decreases very rapidly when the temperature exceeds 800 K, causing the weak signal in S(0). For the next set of experiments, a few changes were made. First of all, point measurements were done to improve the overall signal intensity. Secondly, filamentation was used to extend the excitation bandwidth, making it possible to also observe S(2) and S(3) of Hydrogen.

5.3. Ultra-broadband point measurements

The second set of experiments were ultra-broadband point measurements. In these experiments, the first four S-branch transitions in Hydrogen could be observed, possibly making spectral fitting more accurate and robust. Compared to the line measurements, the signal intensity was much stronger, and only 2x2 pixel binning was required. The data was again recorded in single-shot mode at a 1 kHz repetition rate. Data was gathered at a number of different positions in the flame, ranging from low temperatures zones to high temperature zones to try and find the best conditions for hydrogen signal intensity. Figure 5.5 shows the various measurement positions in the center of the inner flame cone. The first measurement position was the lowest point in the figure, after which the probe volume was moved up 2 mm for each consecutive measurement, gradually moving to a hotter part of the flame.

Figure 5.5: The various measurement positions in the flame.

The figures below show the average spectra as they were recorded by the camera for two different measurement positions. This data has not yet been normalized to show the signal-to-noise ratio's.

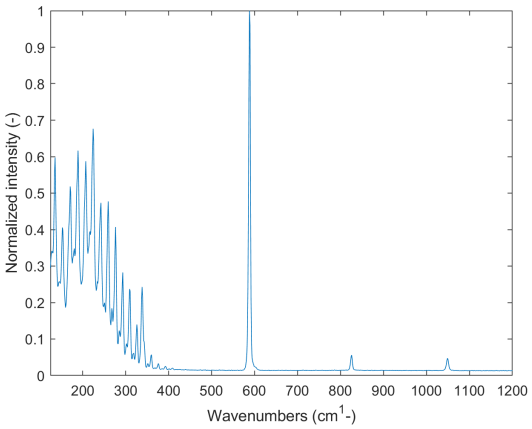

Figure 5.6: The average recorded data at position 5.

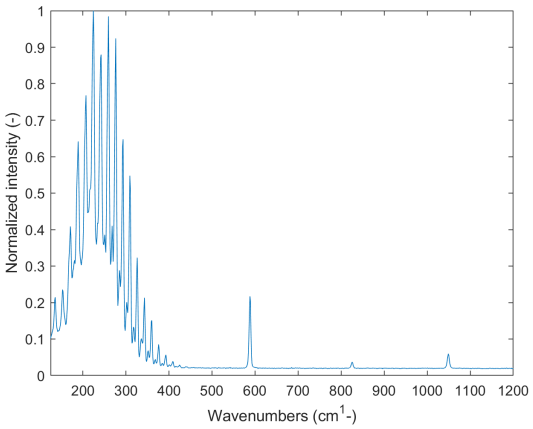

Figure 5.7: The average recorded data at position 10.

The Nitrogen and Air signals can clearly be seen on the left. S(0) of Hydrogen shows up on pixel number 290, but is sometimes obscured by S(43) of Nitrogen. The other three Hydrogen peaks are clearly visible. In the first 5 positions, the signals are quite similar. From position 6 onwards, S(1) of Hydrogen decreases in relative intensity with respect to S(2) and S(3), indicating higher temperatures. This is also confirmed by the shifting of the spectral envelope of the Nitrogen/Oxygen signal. Moving up even further in the flame, the signal-to-noise ratio for the Hydrogen peaks decreases to the point that S(2) can barely be identified at all.

Like with all other experiments, the non-resonant signal was measured in Argon to determine the excitation efficiency required for normalization. A series of 100 frames were recorded to determine the average excitation efficiency. Figure 5.8 shows the variation in the non-resonant signal from shot to shot. In the region where hydrogen is excited, the excitation efficiency varies by as much as 40%. This can in part be explained by the filamentation process. The self-phase modulation which is responsible for frequency broadening the pulse is dependent on the local density of the medium[36]. The filament is created in the flame, where the local density and temperature fluctuate a lot. Another aspect to this issue is the fact that during the CARS measurements the filament was produced in the flame, where the density is different than the Argon in which the non-resonant signal was measured.

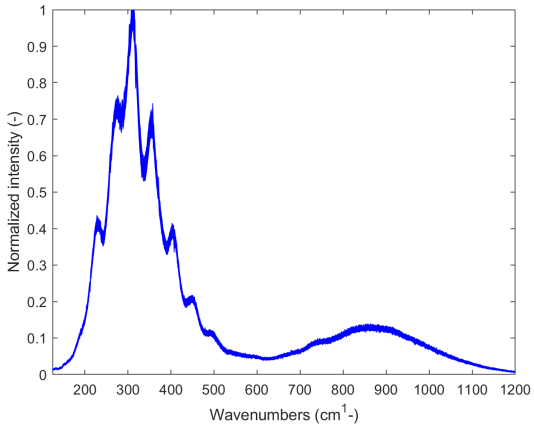

Figure 5.8: The variation in excitation efficiency from shot to shot.

Figure 5.9 shows a best fit for the synthetic nitrogen/oxygen spectrum and the experimental data. As can be seen, the figure is hardly a perfect fit. The data is overestimated in some points, but underestimated in other parts, possibly caused by normalization with incorrect data. Another unrealistic part of the fit is the combination of a high temperature with a high oxygen concentration. Figure 5.10 shows a fit between the recorded experimental data and the synthetic spectrum for hydrogen. As can be seen, the temperature evaluated by the Hydrogen thermometry is much lower than the Nitrogen thermometry predicts.

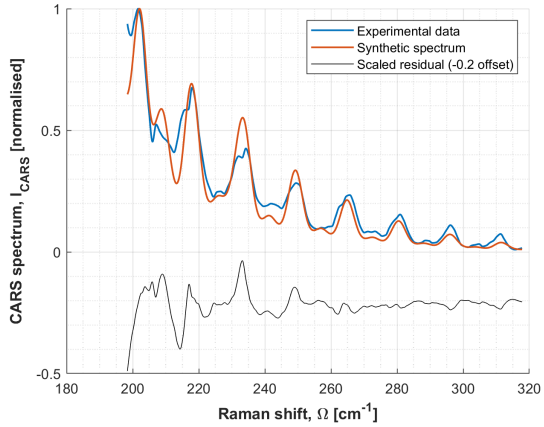

Figure 5.9: Nitrogen/oxygen fitting of a random frame (1028 K and 21% oxygen).

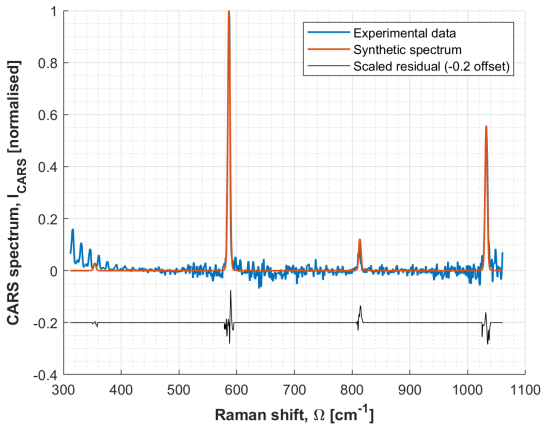

Figure 5.10: Hydrogen fitting (762 K)

Figures 5.11 through 5.32 show the temperatures evaluated using both nitrogen and hydrogen thermometry for measurement positions 1 through 11, during a measurement time of 3 seconds. As can be seen from the data, the hydrogen thermometry consistently underestimates the temperature compared to the nitrogen thermometry. Even though there is a large temperature discrepency, the two data sets seem to follow the same trends. The 1 kHz repetition rate with which the measurements were performed allows meaningful assessment of the auto-correlation of the temperature data, which is not typically possible for CARS measurements. Auto-correlation is the correlation of a signal with a delayed copy of itself, which is a useful tool for finding patterns in data obscured by noise. The auto-correlation function is given in equation 5.1, where τ is the lag time and R is the autocovariance.

$$\rho(\tau) = \frac{R(\tau)}{R(0)} = \frac{\overline{T'(t)T'(t+\tau)}}{\overline{T'^2}} \tag{5.1}$$

The auto-correlation plots (correlograms) presented below show the degree of correlation of the signal with increasingly delayed versions of itself. Per definition, the first value is always 1, because the signal is being compared to itself (undelayed). The second value in the correlograms may experience a discontinuity, which is caused by an instantaneous measurement error. The measured temperature fluctuation $T'_m(t)$ can be seen as the combination of the true temperature fluctuation and some error (equation 5.2).

$$T'_m(t) = T'(t) + n'(t) \tag{5.2}$$

Substituting $T'_m(t)$ for $T'(t)$ into equation 5.1 yields the expression for the measured auto-correlation function (equation 5.3).

$$\rho_m(\tau) = \frac{\overline{\Big(T'(t)+n'(t)\Big)\Big(T'(t+\tau)+n'(t+\tau)\Big)}}{\overline{\Big(T'(t)+n'(t)\Big)^2}} = \rho(\tau)\cdot\frac{1}{1+\frac{\overline{n'^2}}{\overline{T'^2}}} \tag{5.3}$$

This jump in continuity is a direct indicator of the instantaneous measurement error in the data (otherwise known as the precision of the measurement) and can easily be calculated. When calculating the auto-correlation function for two different signals, the degree in similarity between the two auto-correlation functions also pertains to the correlation of the signals. For all signals, the precision and the linear correlation coefficients are calculated, as well as the chance of observing the null hypothesis.

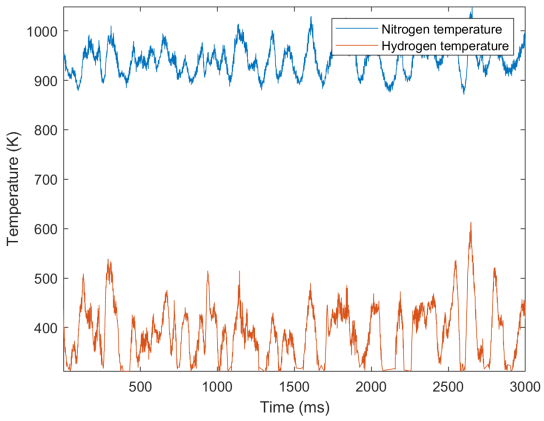

Figure 5.11: Evaluated temperature for N_2 and H_2 at position 1.

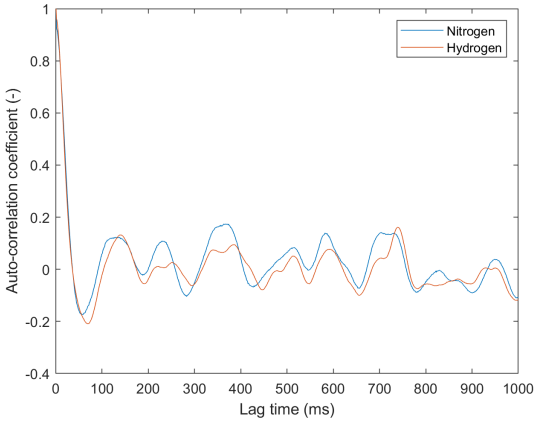

Figure 5.12: Auto-correlations for N_2 and H_2 at position 1.

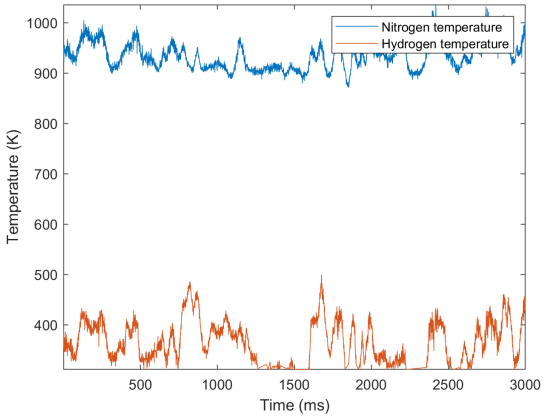

Figure 5.13: Evaluated temperature for N_2 and H_2 at position 2.

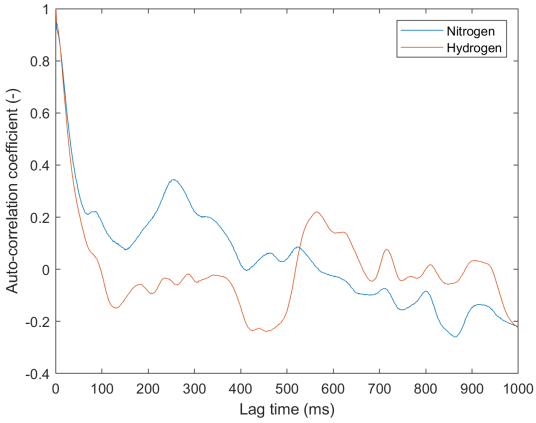

Figure 5.14: Auto-correlations for N_2 and H_2 at position 2.

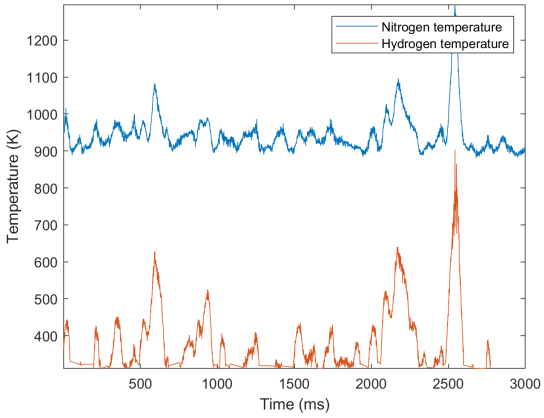

Figure 5.15: Evaluated temperature for N_2 and H_2 at position 3.

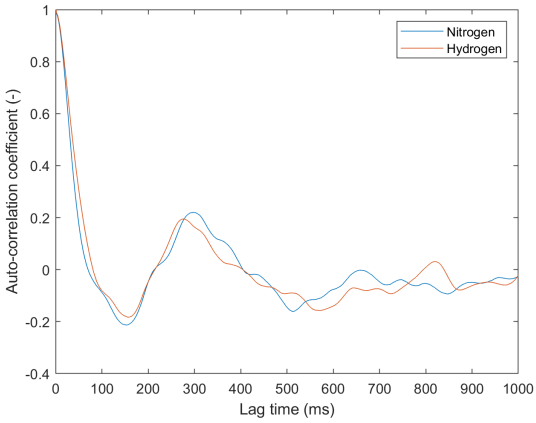

Figure 5.16: Auto-correlations for N_2 and H_2 at position 3.

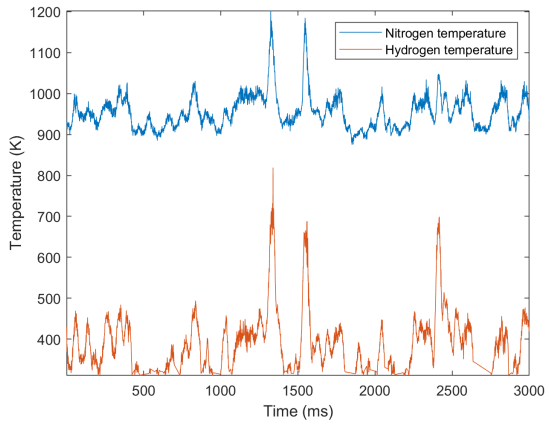

Figure 5.17: Evaluated temperature for N_2 and H_2 at position 4.

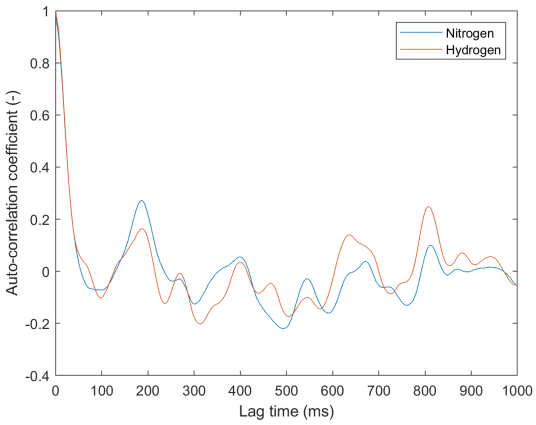

Figure 5.18: Auto-correlations for N_2 and H_2 at position 4.

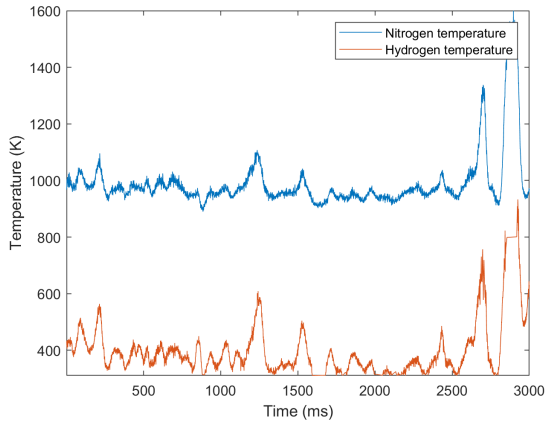

Figure 5.19: Evaluated temperature for N_2 and H_2 at position 5.

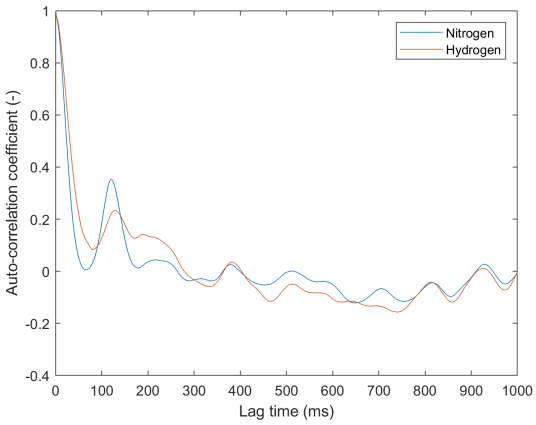

Figure 5.20: Auto-correlations for N_2 and H_2 at position 5.

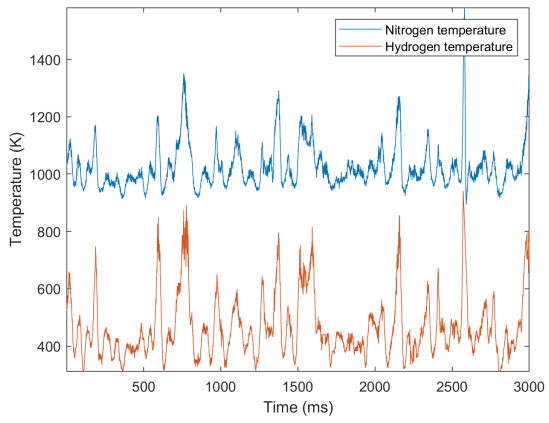

Figure 5.21: Evaluated temperature for N_2 and H_2 at position 6.

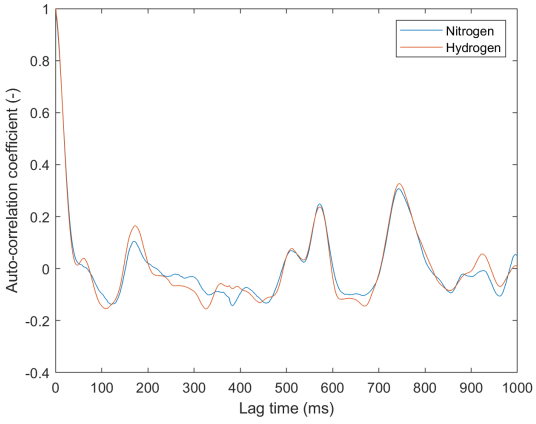

Figure 5.22: Auto-correlations for N_2 and H_2 at position 6.

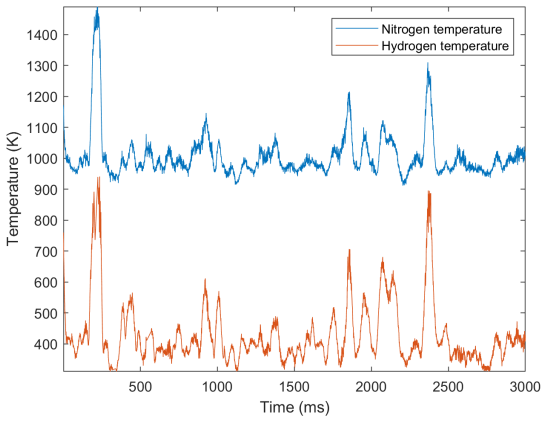

Figure 5.23: Evaluated temperature for N_2 and H_2 at position 7.

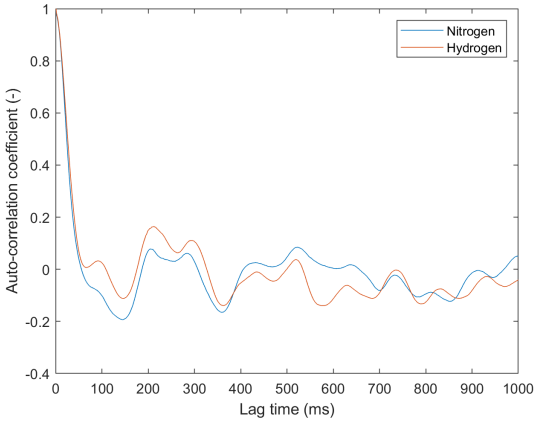

Figure 5.24: Auto-correlations for N_2 and H_2 at position 7.

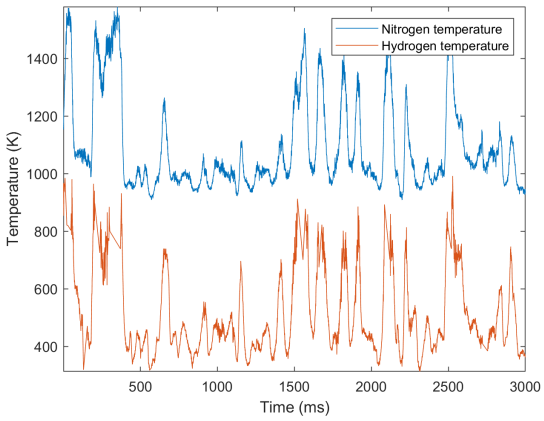

Figure 5.25: Evaluated temperature for N_2 and H_2 at position 8.

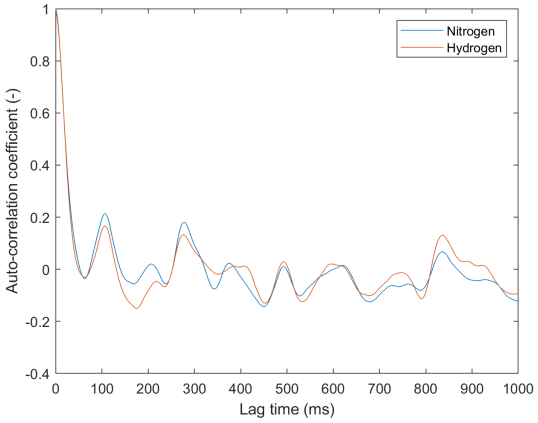

Figure 5.26: Auto-correlations for N_2 and H_2 at position 8.

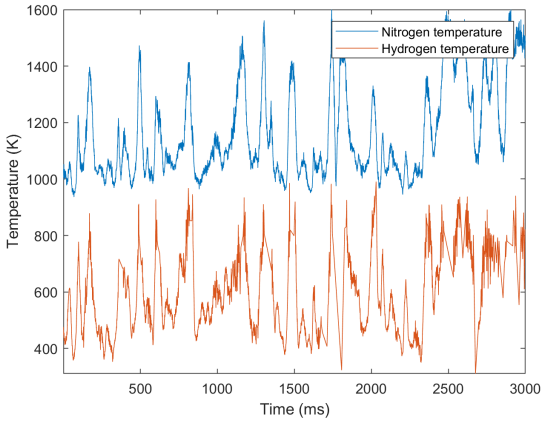

Figure 5.27: Evaluated temperature for N_2 and H_2 at position 9.

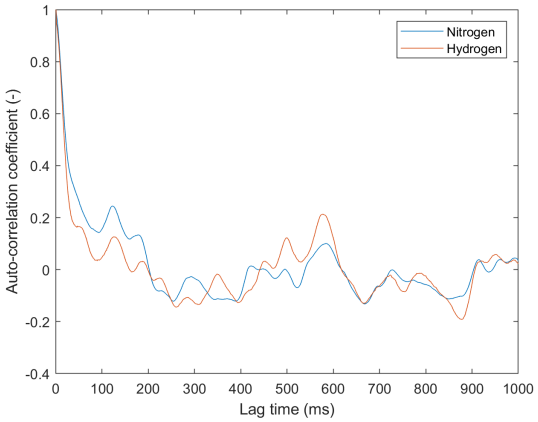

Figure 5.28: Auto-correlations for N_2 and H_2 at position 9.

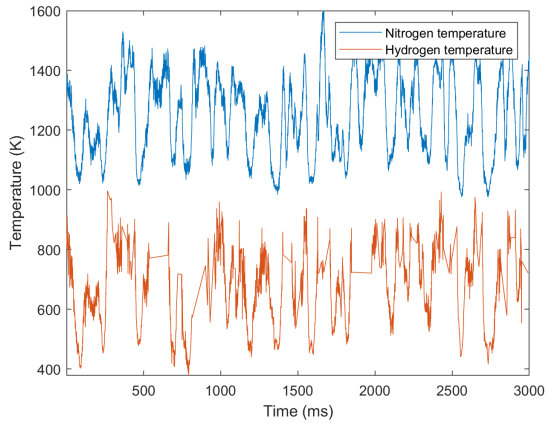

Figure 5.29: Evaluated temperature for N_2 and H_2 at position 10.

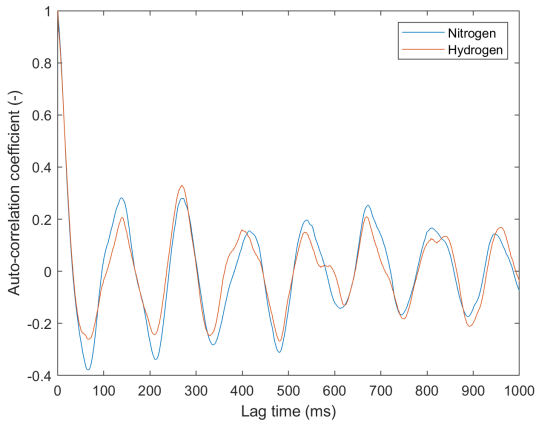

Figure 5.30: Auto-correlations for N_2 and H_2 at position 10.

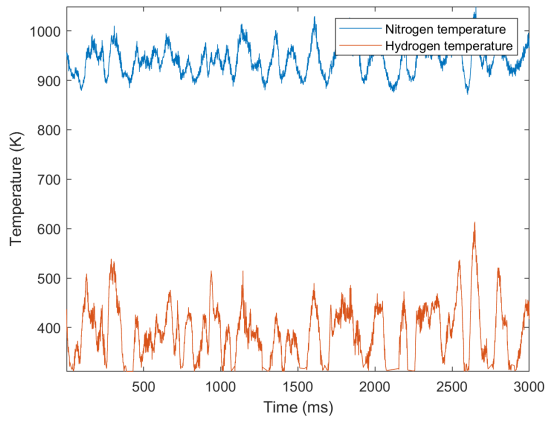

Figure 5.31: Evaluated temperature for N_2 and H_2 at position 11.

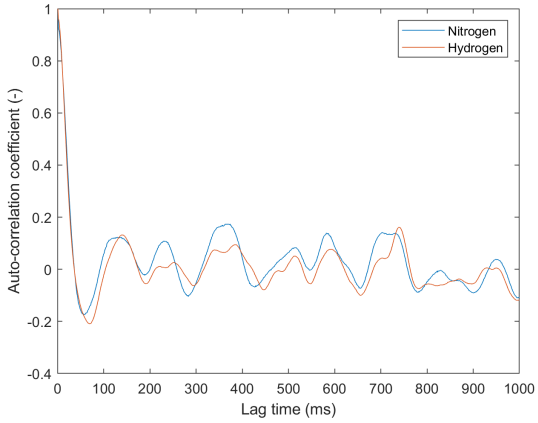

Figure 5.32: Auto-correlations for N_2 and H_2 at position 11.

Position	Average temperatures T_{avg,H_2}, T_{avg,N_2}	Precision T_{H_2}, T_{N_2}	Correlation
1	399.7 K, 949.3	4.1 %, 8.1 %	0.70
2	373.7 K, 940.1 K	5.5 %, 8.5 %	0.39
3	406.9 K, 963.0 K	1.3 %, 1.7 %	0.90
4	403.1 K, 966.8 K	2.6 %, 4.7 %	0.83
5	395.9 K, 981.3 K	2.2 %, 2.5 %	0.86
6	463.9 K, 1022.7 K	2.5 %, 3.5 %	0.90
7	426.7 K, 1003.0 K	1.8 %, 2.6 %	0.87
8	496.5 K, 1052.0 K	2.6 %, 1.5 %	0.90
9	578.5 K, 1116.3 K	5.8 %, 2.0 %	0.85
10	650.7 K, 1192.3 K	8.5 %, 3.6 %	0.83
11	684.0 K, 1172.3 K	7.3 %, 5.4 %	0.83

Table 5.1: The average evaluated temperatures, the precision of the temperature measurements and the linear correlation coefficients for all measurement positions. The null hypothesis was rejected with at least 95% certainty in all cases.

As can be seen from both the linear correlation coefficients and the auto-correlations, there is an unmistakable connection between the evaluated temperatures, even with the large temperature discrepency. These seemingly random fluctuations could be caused by the varying excitation efficiency, which in turn is caused by fluctuations in the local density. One way to overcome this is to simultaneously measure the non-resonant signal with the resonant signal for each recorded frame, in order to accurately compensate for these fluctuations.

There are a few possible explanations as to why there is such a large but consistent difference in temperature evaluated by the Nitrogen and Hydrogen thermometry. A certain ellipticity was observed in the polarization of the signal, which scales with Raman shift. The half wave plates that are used in the setup change the polarization of the light passing through, but this change in polarization is slightly wavelength dependent. For signal at higher Raman shifts therefore has a slightly different polarization than the signal at lower Raman shifts. A number of components in the setup, such as the transmission grating, are also polarization sensitive, reducing the intensity more the higher Raman shifted signal is. When using polarizing filters in the setup (for example for polarization based filtering of the probe or the non-resonant signal) the ellipticity in the polarization will cause the signal to be split among both channels meaning a part of the signal gets discarded. This will affect the Hydrogen signal more, as it is more Raman shifted than the nitrogen signal. Additionally, it will affect the higher S-branch transitions more. When measuring up to S(3) in hydrogen, the evaluated temperature becomes most reliant on the ratio between S(1) and S(3), as they are the strongest peaks. This ratio is also the most sensitive on S(3) as it is the weaker signal of the two. S(3) is affected most by the ellipticity in this signal and a lower measured value for S(3) does in fact translate to a lower evaluated temperature. A solution could be to use a fresnel rhomb in place of traditional half wave plates, as fresnel rhombs do not have the same wavelength dependence.

Another effect that plays a minor role is the mixing of the S(0) and S(43) peaks of Hydrogen and Nitrogen. When evaluating the Hydrogen temperature, a higher value for S(0) translates to a lower temperature.

The transmission grating used in the setup has a transmission efficiency that is dependent on both wavelength and angle of incidence. The corresponding efficiency curves are not gradual or uniform, and efficiency can fall off rapidly past a certain wavelength depending on its orientation. It is possible the grating was placed in such a way that decreased the hydrogen signal intensity of the higher J-lines in Hydrogen, thus leading to a lower evaluated temperature.

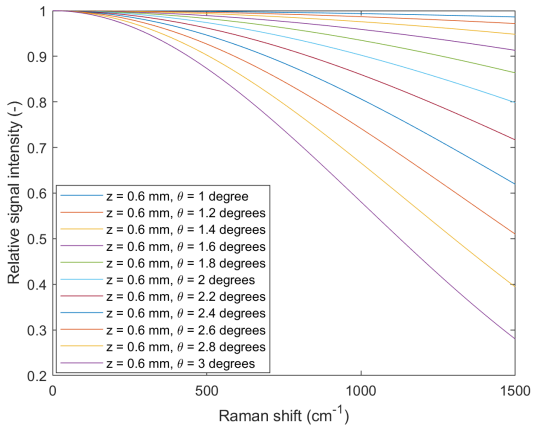

Figure 5.33: The effect of the crossing angle on the decrease in signal intensity.

Another effect that is significant for signals with a large Raman shift is the phase mismatch. This effect grows exponentially the higher Raman shifted a signal is and the larger the crossing angle is. This effect was taken into account, but as figure 5.33 shows, even a slight error in measuring the crossing angle can lead to a large difference in signal intensity.

5.4. Broadband point measurements

After seeing the instabilities in the excitation efficiency with filamentation, the next set of experiments were aimed at obtaining a much more stable and robust signal. Broadband point measurements were used to have a more stable excitation efficiency compared to the ultra-broadband measurements, and still a higher signal intensity compared to the CARS imaging. This did mean however, that again only S(0) and S(1) could be excited. To make thermometry work on just those two peaks, the temperature would have to be low and signal intensity very high. To this end, a few arbitrary measurement positions were chosen low in the inner

flame cone. The data that was recorded during these experiments had much higher signal-to-noise ratio's than observed before, and the data could be recorded in single shot mode at a 1 kHz repetition rate without any binning. Figure 5.34 shows a random recording from the dataset, showing a clear signal for both S(0) and S(1).

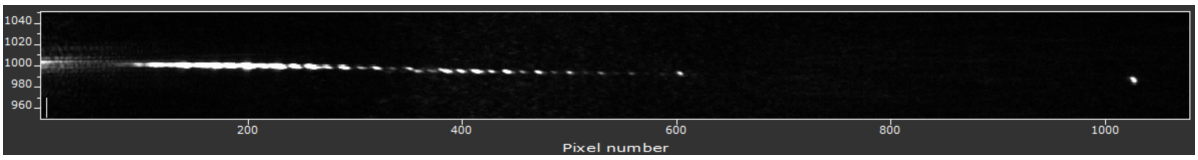

Figure 5.34: An example of the recorded data using broadband point measurements.

To check whether the excitation efficiency was indeed more stable without the filamentation, the variation in the non-resonant signal was inspected again. Figure 5.35 still shows some fluctuations in the non-resonant signal, but far less than for the ultra-broadband excitation. The lack of signal in the area up to pixel number 400 is due to a neutral density filter that was placed here. This obscured some of the Nitrogen data, but was necessary to prevent the signal from saturating the camera.

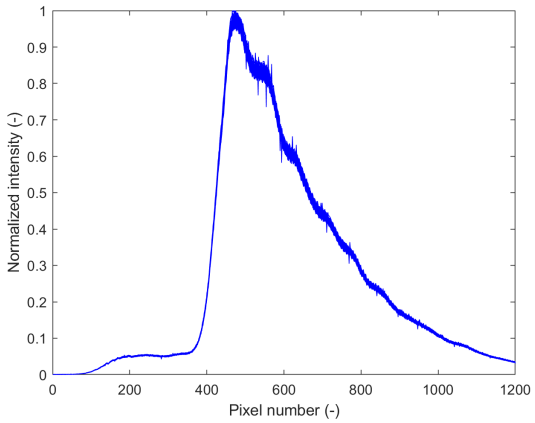

Figure 5.35: The variation in the non-resonant signal recorded in Argon.

The figures below show two example normalized spectra from the dataset. The clear signal in the camera and the decent excitation efficiency lead to clear normalized spectra, that can easily be fitted.

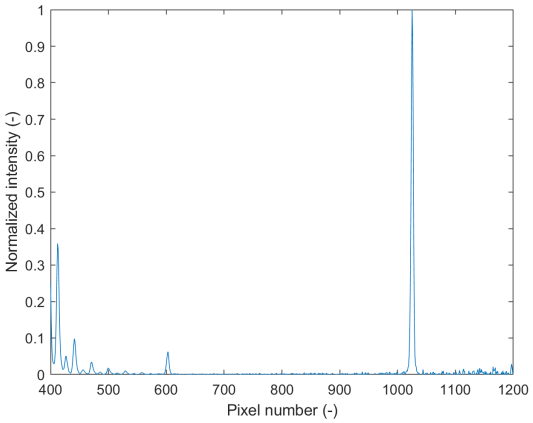

Figure 5.36: Normalized spectrum at position 1

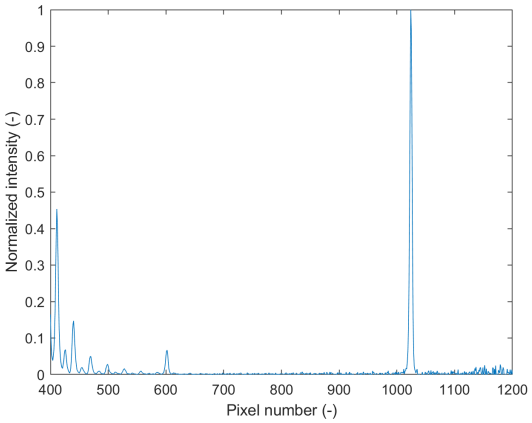

Figure 5.37: Normalized spectrum at position 2

Figure 5.38 shows a typical fit from the flame data from these experiments. To negate the effect that the bandpass filter might have, the lower J-lines for nitrogen are disregarded. Figure 5.39 shows the fitting of the

same data as in figure 5.38, but now using the synthetic spectrum for hydrogen. The problem encountered in figure 5.10 is also evident here, but to a lesser degree. Looking closely at the signal surrounding S(0) in figure 5.39 reveals some weak signal from Nitrogen S(43), effectively increasing the evaluated signal for S(0). Because of the high sensitivity of the temperature on the intensity of S(0), even such a small influence is enough to lead to a lower evaluated temperature.

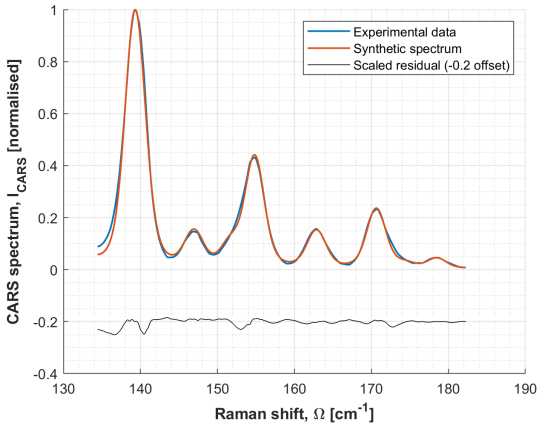

Figure 5.38: Nitrogen/oxygen fitting (466 K and 17.5 % oxygen).

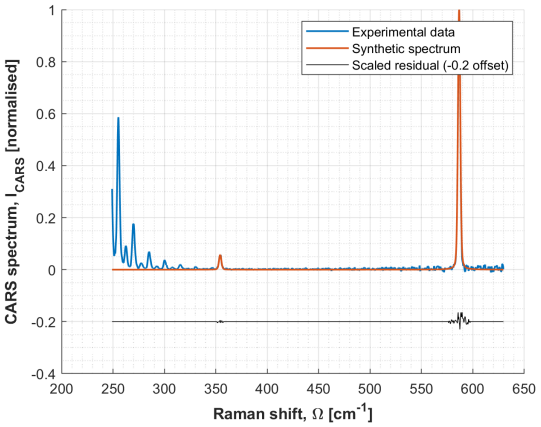

Figure 5.39: Hydrogen fitting (390 K).

Figures 5.40 through 5.43 again show temperatures evaluated with both nitrogen and hydrogen thermometry for 2 arbitrary positions in the flame during a measurement time of 2 seconds. The average temperatures are much closer together this time, but the hydrogen temperature is fluctuating a lot while the nitrogen temperature is much more steady. Again, the auto-correlation functions and correlation coefficients were determined.

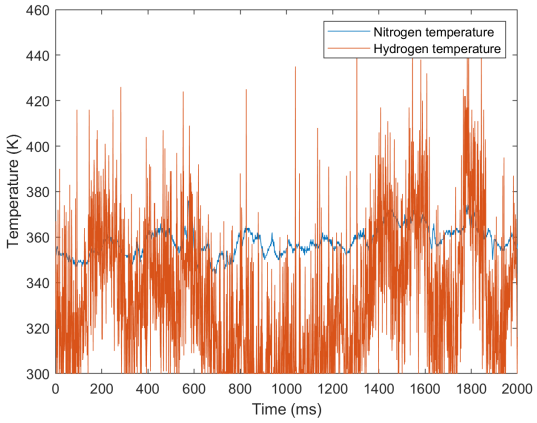

Figure 5.40: Evaluated temperature for N_2 and H_2 at position 1.

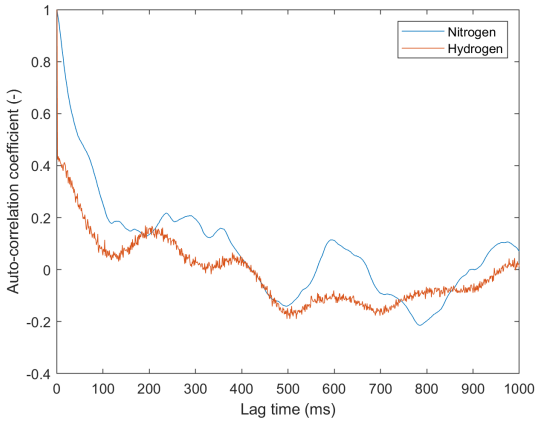

Figure 5.41: Auto-correlations for N_2 and H_2 at position 1.

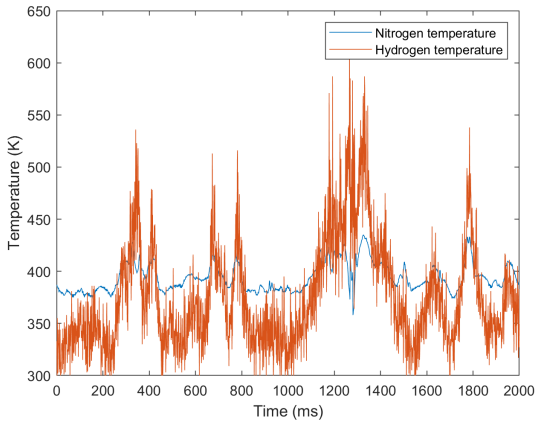

Figure 5.42: Evaluated temperature for N_2 and H_2 at position 2.

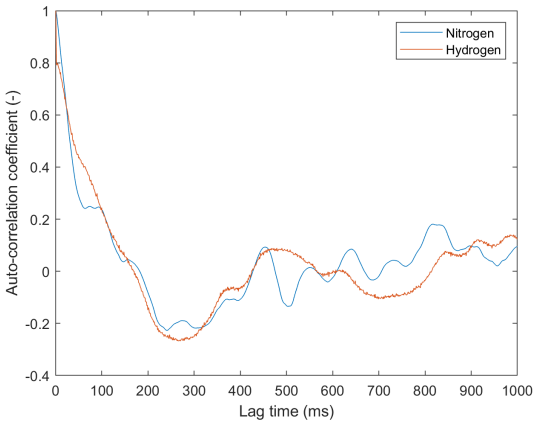

Figure 5.43: Auto-correlations for N_2 and H_2 at position 2.

Position	Average temperatures T_{avg,H_2}, T_{avg,N_2}	Precision T_{H_2}, T_{N_2}	Correlation
1	333.7 K, 358.1.0	22.6 %, 1.8 %	0.42
2	375.8 K, 394.0 K	25.4 %, 1.2 %	0.75

Table 5.2: The average evaluated temperatures, the precision of the temperature measurements and the linear correlation coefficients for both measurement positions. The null hypothesis was rejected with at least 95% certainty in both cases.

The unsteady behaviour could be explained by the combined effect of the mixing of S(43) and S(0) and the slight variations in excitation efficiency. If line mixing occurs and the excitation efficiency in that shot happens to be slightly higher for S(0), a much lower temperature is evaluated. On the other hand, if no line mixing occurs and the excitation efficiency is slightly lower in that shot, a higher temperature is evaluated. Even though the average temperature is much more closely matched compared to the experiments using ultra-broadband excitation, the precision is much lower when only S(0) and S(1) are measured. Even though the precision is low, there is still a moderate correlation between hydrogen and nitrogen temperature in position 1 and a good correlation between the temperatures in position 2.

5.5. Ultra-broadband CSRS measurements

Initially, the idea was to solely do measurements on the CARS side (S-branch) because the theory indicated the signal would be stronger there. However, during experiments performed by another master student in our group (Nathan Griffioen under supervision of Francesco Mazza) on the O-branch of CO_2 he discovered very strong hydrogen signals. These signals were discovered at lower equivalence ratio's and on the CSRS side, where the theory indicates the signal should be much weaker. The post-doctoral researcher in our group (Dmitrii Kliukin) then started looking specifically for hydrogen on the CSRS side of the spectrum in the products side of the flame and was able to record hydrogen signals from O(3) to O(7). The results presented below were processed from his experimental data. The figure below shows the O-branch signal as it was recorded in the camera. On the right is the signal from O(3), with O(7) barely visible on the far left. The data was recorded in single shot mode, at a repetition rate of 1 kHz with no pixel binning.

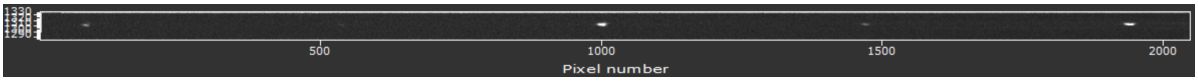

Figure 5.44: An example of the recorded data from the Hydrogen O-branch.

Figure 5.45 shows the variation in the non-resonant signal shot to shot, which varies by 20-25%. Interestingly, the excitation bandwidth on the CSRS side is much higher and more uniform than what was seen before on the CARS side. To make an unbiased comparison, the same settings were used to record data on both sides of the spectrum. The comparison between the non-resonant signals for the CSRS and CARS side is shown in figure 5.46.

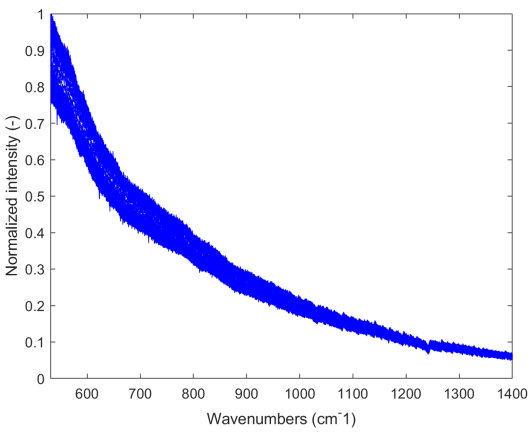

Figure 5.45: The variation in the non-resonant signal for the CSRS side

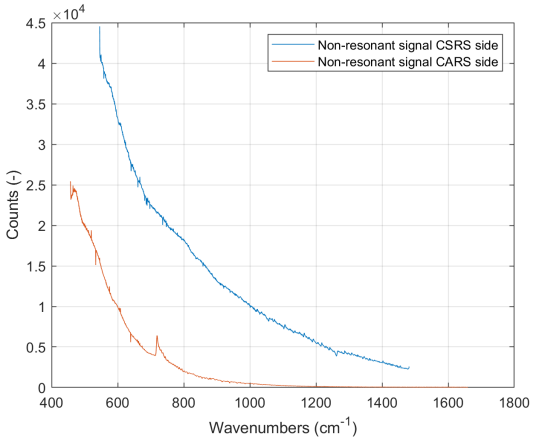

Figure 5.46: Average non-resonant data for the CARS and CSRS side of the spectrum.

Since the pulse shape of the pump/Stokes beam is roughly Gaussian, the expected bandwidth on both sides of the spectrum is equal. The difference might be caused again by wavelength dependence in the used optics, which are optimized for 400 nm. Depending on the application and manufacturer, the transmission efficiency outside the intended wavelength can vary greatly.

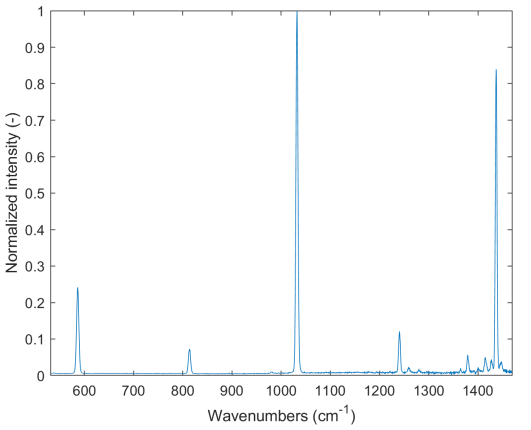

Figure 5.47: The average normalized Hydrogen O-branch spectrum.

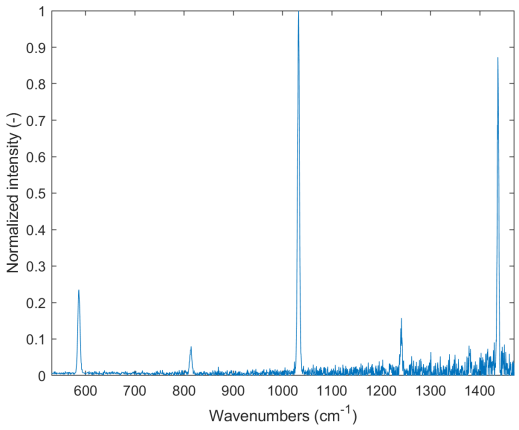

Figure 5.48: The normalized spectrum for a random frame.

After obtaining the non-resonant signal, the data can be normalized. Figure 5.47 shows the average normalized spectrum, and figure 5.48 shows the normalized spectrum from a random frame. These spectra are inverted from the camera data that was shown earlier, with O(3) now on the left and O(7) on the right. Around 1350 wavenumbers some CO_2 lines can be identified, but the signal is otherwise fairly isolated.

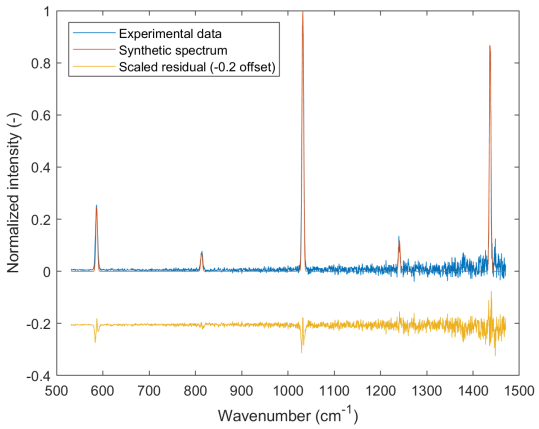

Figure 5.49: A best fit for a random frame (2000 K).

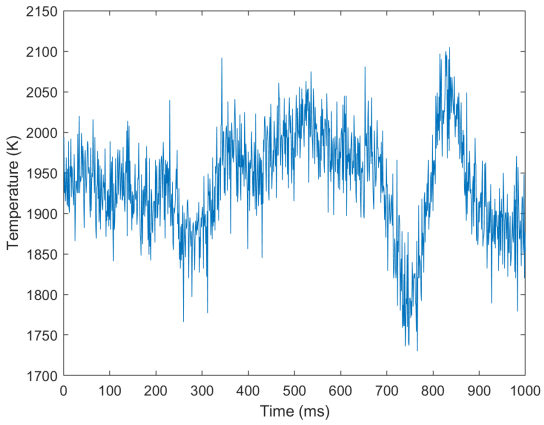

Figure 5.50: Hydrogen O-branch thermometry versus time.

Figure 5.49 shows the best fit for a random frame in the dataset, evaluated at 2000 K. Figure 5.50 shows the temperature of all frames, the average of which is 1937 K. The equivalence ratio for the corresponding flame was 1.24, which equates to an adiabatic flame temperature of 2100 K. Nitrogen spectra were also recorded and evaluated at 2076 K. It should be noted that the adiabatic flame temperature is a maximum ideal value, and the actual flame temperature is likely a bit lower due to heat transfer effects. Compared to the Nitrogen temperature, the Hydrogen temperature is 7% lower. This difference is possibly caused by the effects of phase mismatching depicted in figure 5.33 which especially O(7) is very sensitive to. Fourier analysis of the temperature data from figure 5.50 shows no dominant frequencies. These fluctuations are possibly caused by the variations in the excitation bandwidth. To improve the accuracy of these measurements, dual channel recording can be applied to simultaneously record the resonant and non-resonant spectrum for each shot.

6

Conclusions and outlook

At the beginning of this report, a research question was posed along with three sub questions to help structure the report. This chapter aims to answer those questions and give recommendations for future research.
The results presented in the previous chapter clearly show it is possible to do multi-species measurements on both Hydrogen and Nitrogen. The spectra were distuinghishable from one another and fitting could be performed independently for both species. That being said, there is still a lot to gain in this area. The difference in relative concentration between the Nitrogen and Hydrogen was large, which caused a large difference in signal intensity. Optimizing for the hydrogen signal meant saturating the Nitrogen signal, and optimizing for the Nitrogen signal meant having a weak Hydrogen signal, leading to larger inaccuracies. Filters were used to try and equalize the signal intensities, but any additional optics introduce additional inaccuracies and uncertainties. If these measurements were to be redone, it would help to mix in additional pure hydrogen. The use of filters during the experiments proved troublesome and should be avoided if possible.

The two-beam hybrid fs/ps CARS setup as it currently exists in the lab is able to excite multiple rotational transitions in Hydrogen. The standard 35 fs output of the regenerative amplifier can be used to excite S(0) and S(1) in Hydrogen. Performing thermometry solely on S(0) and S(1) is highly dependent on S(0), and therefore the accuracy with which it can be measured. Small changes in the S(0) signal lead to large changes in temperature predicted by the model. Additionally, the higher the temperature, the lower the population of S(0) will become, until the signal cannot be distinguished. This means that there exists an upper limit for the temperature at which S(0) can be measured at all, but this depends also on the amount of noise, the excitation efficiency and any other signals that might be present at this Raman shift. In theory, as few as two hydrogen peaks can be used for accurate thermometry, but this strongly depends on the quality of the signal.

The compressed 10 fs pulse was able to probe up to S(3) in hydrogen on the CARS side. The two additional available peaks in the hydrogen spectrum significantly increased the precision of the thermometry, because it was not only dependent on the highly sensitive ratio between S(0) and S(1). Instead, the evaluated temperature became most dependent on S(1) and S(3), being the strongest peaks in the spectrum. S(1) was barely distinguishable and often overlapped with S(43) in nitrogen. Furthermore, any effects that scale with wavelength, such as the induced polarization of the half-wave plates, affect S(3) much more than the rest of the signal, leading to consistently under-evaluated hydrogen temperatures.

On the CSRS side up to O(7) was recorded using the 10 fs pulse, with sufficient excitation bandwidth to excite even higher states. These experiments evaluated the hydrogen temperature much closer, coming within 7% of the measured nitrogen temperature. There is a significant discrepency in excitation bandwidth between the CARS and CSRS sides of the spectrum however, an issue that will have to be investigated further.

While performing thermometry on higher J-lines in the spectrum, the influence of phase mismatching must be taken very seriously. The phase mismatch is inherent to using a two-beam CARS setup, and affects the hydrogen spectrum severely. Additionally, using a two-beam CARS setup means that extra measures have to be taken to separate the signal from the probe, most of these measures involving sacrificing signal intensity. Performing the same measurements on a three-beam CARS setup introduces additional alignment difficul-

ties, but eliminates the influence of phase mismatching and physically separates the signal from the probe.

Especially during the experiments where ultra-broadband excitation was used, the non-resonant signal in Argon was varying. The use of self-referencing would eliminate this problem and possibly reduce the seemingly random fluctuations in the evaluated temperature. A number of components in the setup are polarization sensitive, and the CARS signal was measured to be elliptically polarized. This means different portions of the signal are affected differently by the various optical components, skewing the final data. In these experiments, the half-wave plates induced a wavelength dependent polarization. This can be prevented by using fresnel rhombs, which induce a difference in polarization that is independent on wavelength.

Clear correlations where seen between evaluated Hydrogen and Nitrogen temperatures, but also clear discrepancies. There is a possible explanation for these discrepancies, so more research is needed to either confirm or deny these hypotheses. All in all, the results obtained during this research were promising, but not yet conclusive and more research is needed.

Bibliography

[1] L.E. Klebanoff, J.W. Pratt, C.B. Lafleur, *Comparison of the Safety-related Physical and Combustion Properties of Liquid Hydrogen and Liquid Natural Gas in the Context of the SF-BREEZE High-Speed Fuel-Cell Ferry*, Sandia National Laboratories.

[2] Gavin A. Schmidt, Reto A. Ruedy, Ron L. Miller, Andy A. Lacis, *Attribution of the present-day total greenhouse effect*, JOURNAL OF GEOPHYSICAL RESEARCH, VOL. 115, D20106, doi:10.1029/2010JD014287, 2010.

[3] Andrew A. Lacis, Gavin A. Schmidt, David Rind, Reto A. Ruedy, *Atmospheric CO_2: Principal Control Knob Governing Earth's Temperature*, SCIENCE, VOL 330, 15 OCTOBER 2010.

[4] R. Umair Shahzad, *Global Warming: Causes, Effects and Solutions*, Durreesamin Journal (ISSN: 2204 - 9827), August Vol 1 Issue 4, Year 2015.

[5] Data Statistics, `https://www.iea.org/data-and-statistics?country=WORLD&fuel=CO2%20emissions&indicator=CO2%20emissions%20by%20sector`, International Energy Agency, 2019.

[6] A. De Santis, D.B. Ingham, L. Ma, et al., *CFD analysis of exhaust gas recirculation in a micro gas turbine combustor for CO2 capture. Fuel*, 173. C. pp. 146-154. ISSN 0016-2361, 2016.

[7] M. Balat, *Potential importance of hydrogen as a future solution to environmental and transportation problems*, International Journal of Hydrogen Energy 33, 4013 – 4029, (2008).

[8] C.Y. She, *Spectral structure of laser light scattering revisited: bandwidths of nonresonant scattering lidars*, APPLIED OPTICS, Vol. 40, No. 27, 20 September 2001.

[9] M. Marrocco, *Herman–Wallis factor to improve thermometric accuracy of vibrational coherent anti-Stokes Raman spectra of H2*, Proceedings of the Combustion Institute 32, pp 863–870, 2009.

[10] Collisional Broadening, `https://sciencedemonstrations.fas.harvard.edu/presentations/collisional-broadening`, Harvard Natural Sciences

[11] E. Novotny, *Introduction to Stellar Atmospheres and Interiors*, Oxford University Press, pp 206 - 210, 1973.

[12] G. Livadiotis, *Thermal Doppler Broadening of Spectral Emissions in Space and Astrophysical Plasmas*, The Astrophysical Journal Supplement Series, 239:25, (21pp), December 2018.

[13] J. Wang, *Dicke narrowing and speed-dependent effects in dispersion signals*, Doctoral Thesis, Department of Physics, Umeå University, Sweden, 2013.

[14] W. M. Tolles, J. W. Nibler, J. R. McDonald, A. B. Harvey, *A Review of the Theory and Application of Coherent Anti-Stokes Raman Spectroscopy (CARS*, APPLIED SPECTROSCOPY, Volume 31, Number 4, 1977.

[15] Nelson L. Alpert, William E. Keiser, Herman A. Szymanski, *IR: Theory and Practice of Infrared Spectroscopy*, Springer, Chapter 4, p 91, 1970.

[16] Rotational Spectroscopy of Diatomic Molecules, `https://chem.libretexts.org/Bookshelves/Physical_and_Theoretical_Chemistry_Textbook_Maps/Supplemental_Modules_(Physical_and_Theoretical_Chemistry)/Spectroscopy/Rotational_Spectroscopy/Rotational_Spectroscopy_of_Diatomic_Molecules`

[17] A. Bohlin, *Development and Application of Pure Rotational CARS for Reactive Flows*, Lund University, Doctoral Thesis, 2012.

[18] I. R. McNab, *Encyclopedia of Spectroscopy and Spectrometry (Third Edition)*, Theory of Rotational Spectroscopy, Pages 978-987, 2017.

[19] C. Pasquini, *Near Infrared Spectroscopy: Fundamentals, Practical Aspects and Analytical Applications*, J. Braz. Chem. Soc., Vol. 14, No. 2, 198-219, 2003.

[20] T. A. Fayed, Microwave (Rotational) Spectroscopy, Tanta University Egypt, obtained from `http://sci.tanta.edu.eg/files/Microwave%20spectroscopy%20BSc-Lect-2.pdf`

[21] R. L. Cook, *Microwave molecular spectroscopy*, Encyclopedia of Physical Science and Technology (Third Edition), Pages 799-852, 2003.

[22] P. A. Tipler, G. P. Mosca, *Physics for scientists and engineers* Chapter 31, Properties of light, New York: W.H. Freeman, 2003.

[23] E. O. Potma, S. Mukamel, *Coherent Raman Scattering Microscopy*, Taylor Francis Group, LLC. ISBN: 978-1-4398-6765-5, Chapter 1 Theory of Coherent Raman Scattering, pages 3 - 41, 2003.

[24] J. D. Miller, *Hybrid femtosecond/picosecond coherent antiStokes Raman scattering for gas-phase temperature measurements*, Doctoral Thesis, Iowa State University, 2012.

[25] C. R. H. de Smet, *Partial oxidation of methane to synthesis gas: reaction kinetics and reactor modelling*, Technische Universiteit Eindhoven, 2000.

[26] Y. Wang, X. He, Y. Li, *Hydrogen formation from methane rich combustion under high pressure and high temperature conditions*, International Journal of Hydrogen Energy 42 (2017), 14301 - 14311.

[27] M. H. Morsy, *Modeling study on the production of hydrogen/ syngas via partial oxidation using a homogeneous charge compression ignition engine fueled with natural gas*, Iternational Journal of Hydrogen Energy 34 (2014) 1096 - 1104.

[28] A. Bohlin, C. J. Kliewer, *Two-beam ultrabroadband coherent anti-Stokes Raman spectroscopy for high resolution gas-phase multiplex imaging*, Applied Physics Letters 104, 031107 (2014).

[29] B. Lemke, C. Roodhouse, N. Glumac, H. Krier, *Hydrogen synthesis via combustion offuel-rich natural gas/air mixtures at elevated pressure*, International Journal of Hydrogen Energy 30 (2005) 893 – 902.

[30] M. H. McMillian, S. A. Lawson, *Experimental and modeling study ofhydrogen/syngas production and particulate emissions from a natural gas-fueled partial oxidation engine*, International Journal of Hydrogen Energy 31 (2006), 847 – 860.

[31] T. L. Courtney, N. T. Mecker, B. D. Patterson, M. Linne, and C. J. Kliewer, *Generation of narrowband pulses from chirped broadband pulse frequency mixing*, Opt. Lett. 44 (2019), 835 - 838.

[32] K. E. Thorn, N. R. Monahan, S. K. K. Prasad, K. Chen, J. M. Hodgkiss, *Efficient and tunable spectral compression using frequency-domain nonlinear optics*, Optics Express Vol. 26, No. 21, (2018), 28140 - 28149.

[33] L. Castellanos, F. Mazza, D. Kliukin, A. Bohlin, *Pure-rotational 1D-CARS spatiotemporal thermometry with a single regenerative amplifier system*, Vol. 45, No. 17 / 1 September 2020 / Optics Letters.

[34] A. Bohlin, B. D. Patterson, C. J. Kliewer, *Communication: Simplified two-beam rotational CARS signal generation demonstrated in 1D*, The Journal of Chemical Physics 138, 081102, 2013.

[35] J. Dahl, *Vibration and Rotation of Diatomic Molecules*, Introduction to the Quantum World of Atoms and Molecules, pp 324 - 340, 2001

[36] M. Gu, A. Satija, R. P. Lucht, *Effects of self-phase modulation (SPM) on femtosecond coherent anti-Stokes Raman scattering spectroscopy*, Vol. 27, No. 23 / 11 November 2019 / Optics Express 33954.

[37] B. D. Prince, *Development and application of a hybrid femtosecond / picosecond coherent Raman probe designed for study of excited state systems*, Doctoral thesis, Iowa State University, 2008.

[38] T. L. Courtney, A. Bohlin, B. D. Patterson, C. J. Kliewer, *Pure-rotational H2 thermometry by ultrabroadband coherent anti-Stokes Raman spectroscopy*, The Journal of Chemical Physics 146, 224202, (2017).

[39] A. Couairon, A. Mysyrowicz, *Femtosecond filamentation in transparent media*, Physics Reports 441, (2007) 47–189.

[40] A. Bohlin, C. J. Kliewer, *Communication: Two-dimensional gas-phase coherent anti-Stokes Raman spectroscopy (2D-CARS): Simultaneous planar imaging and multiplex spectroscopy in a single laser shot*, The Journal of Chemical Physics 138, 221101 (2013).

[41] T. L. Courtney, N. T. Mecker, B. D. Patterson, M. Linne, and C. J. Kliewer, *Hybrid femtosecond/picosecond pure rotational anti-Stokes Raman spectroscopy of nitrogen at high pressures (1–70 atm) and temperatures (300–1000 K)*, Appl. Phys. Lett. 114, 101107 (2019).

[42] A. Bohlin, C. Jainski, B. D. Patterson, A. Dreizler, C. J. Kliewer, *Multiparameter spatio-thermochemical probing of flame–wall interactions advanced with coherent Raman imaging*, Proceedings of the Combustion Institute 36 (2017) 4557–4564.

[43] D. Romanov, *Phase matching in femtosecond BOXCARS*, November 1, 2007 / Vol. 32, No. 21 Optics Letters.

[44] S. Kearney, *Hybrid fs/ps rotational CARS temperature and oxygen measurements in the product gases of canonical flat flame*, Combustion and Flame 162 (2015), 1748–1758.

[45] A. Bohlin, P. Bengtsson, *Effective Suppression of Stray Light in Rotational Coherent Anti-Stokes Raman Spectroscopy Using an Angle-Tuned Short-Wave-Pass Filter*, Applied Spectroscopy, Volume 64, Number 8, 2010.

[46] A. Bohlin, P. Bengtsson, M. Marrocco, *On the sensitivity of rotational CARS N2 thermometry to the Herman–Wallis factor*, Journal of Raman Spectroscopy 2011, 42, 1843–1847.

[47] J. Oudar, R. W. Smith, Y. R. Shen, *Polarization-sensitive coherent anti-Stokes Raman spectroscopy*, Appl. Phys. Lett. 34, 758 (1979).

[48] F. Vestin, M. Afzelius, P. Bengtsson, *Development of rotational CARS for combustion diagnostics using a polarization approach*, Proceedings of the Combustion Institute 31 (2007) 833–840.

[49] J. Kiefer, P. Ewart, *Laser diagnostics and minor species detection in combustion using resonant four-wave mixing*, Progress in Energy and Combustion Science 37 (2011) 525-564.

[50] R. Boyd, *Nonlinear Optics, third edition*, Academic Press, 2008.

[51] N. T. Mecker, *Hybrid rotational femtosecond/picosecond coherent anti-Stokes Raman spectroscopy of Nitrogen at high pressures and temperatures*, Doctoral thesis, University of Edinburgh, 2020.

[52] G. Gangisetty, A. V. T. Jayachandran, V.Y. Sverbilov, I.A Zubrilin, S. S. Matveev, *Review paper on thermoacoustic instabilities in a gas turbine burners – Flashback avoidance*, Journal of Physics: Conf. Series 1276 (2019) 012051.

[53] A. Kalantari, V. McDonell, *Boundary layer flashback of non-swirling premixed flames: Mechanisms, fundamental research, and recent advances*, Progress in Energy and Combustion Science, Volume 61, July 2017, Pages 249-292.

[54] C. Eichler, G. Baumgartner, *Experimental investigation of turbulent boundary layer flashback limits for premixed hydrogen-air flames confined in ducts*, J. Eng. Gas Turbines Power, January 2012, 134.

[55] R. H. Dicke, *The Effect of Collisions upon the Doppler Width of Spectral Lines*, Physical Review Volume 89, Number 2, January 1953.

[56] G. Livadiotis, *Thermal Doppler Broadening of Spectral Emissions in Space and Astrophysical Plasmas*, The Astrophysical Journal Supplement Series, 239:25 (21pp), December 2018.